Strathprints Institutional Repository

A Maximum Eigenvalue Approximation for Crack Sizing using Ultrasonic Arrays

Laura Cunningham[1], Anthony J. Mulholland[1], Katherine M. M. Tant[1], Anthony Gachagan[2], Gerry Harvey[3], and Colin Bird[4]

[1]Department of Mathematics and Statistics, University of Strathclyde, Glasgow, U.K.,G1 1XH

[2]Centre for Ultrasonic Engineering, University of Strathclyde, Glasgow, U.K.,G1 1XW

[3]PZFlex Europe, 50 Richmond Street, Glasgow, UK, G1 1XP

[4]Doosan Babcock, T&E Building, Porterfield Road, Renfrew,Glasgow, UK, PA4 8DJ

May 20, 2015

Abstract

Ultrasonic phased array systems are becoming increasingly popular as tools for the inspection of safety-critical structures within the non-destructive testing industry. The datasets captured by these arrays can be used to image the internal microstructure of individual components, allowing the location

and nature of any defects to be deduced. Unfortunately, many of the current imaging algorithms require an arbitrary threshold at which the defect measurements can be taken and this aspect of subjectivity can lead to varying characterisations of a flaw between different operators. This paper puts forward an objective approach based on the Kirchoff scattering model and the approximation of the resulting scattering matrices by Toeplitz matrices. A mathematical expression relating the crack size to the maximum eigenvalue of the associated scattering matrix is thus derived. The formula is analysed numerically to assess its sensitivity to the system parameters and it is shown that the method is most effective for sizing defects that are commensurate with the wavelength of the ultrasonic wave (or just smaller than). The method is applied to simulated FMC data arising from finite element calculations where the crack length to wavelength ratios range between 0.6 and 1.8. The recovered objective crack size exhibits an error of 12%.

1   Introduction

Non-destructive evaluation (NDE) is the name given to the group of techniques employed to inspect safety critical structures non-invasively. Such structures include oil rigs, nuclear power stations and aircraft [1]. The development of NDE is essential as the detection and characterisation of flaws in such structures can prevent catastrophic failure. Additionally, it is a cost-effective approach as components need only be replaced when a defect occurs within them. Some common NDE technologies include industrial radiography [2], electromagnetic testing [3], laser inspection [4], liquid penetrant testing and ultrasonic testing [5]. Ultrasonic testing is the most widely applicable of these techniques as it is comparatively inexpensive, portable and it can be used for sizing internal defects of various shapes and sizes [6].

1

Piezoelectric transducers [7] are the most widely used and contain an active piezoelectric element which converts the electrical pulse generated into mechanical energy (and vice versa). The elastic wave is emitted from the transducer and travels through the component under inspection. The wave is then reflected and scattered from any obstacles within the component and received by the transducer. In recent years there has been an increase in the use of ultrasonic arrays for NDE inspections [8, 9]. An ultrasonic array is a single transducer that is comprised of a number of piezoelectric elements (typically between 64 and 256), where each element acts as both a transmitter and a receiver. There are several advantages of arrays to conventional ultrasonic probes (a device which contains only a single element); they cover a larger inspection area thus reducing the time taken to conduct an inspection and they can be used to produce a range of ultrasonic fields such as plane, focused and steered beams. The full set of time domain transmitted and received signals recorded by an ultrasonic array is referred to as the Full Matrix Capture (FMC) data. This is a three dimensional (transmitting element, receiving element and time) data block and is generated by firing an ultrasonic wave through one element and then receiving the reflected signal across the entire array. This process is repeated for each element until the entire set of signals is recorded to form the FMC dataset. Once the FMC data has been collected, post processing algorithms are applied to extract information associated with a flaw; this is the inverse problem. Considerable effort has been expended in developing techniques to characterise internal defects via the exploitation of these FMC datasets [10–23]. In particular there has been a series of papers developing the Total Focusing method (TFM) [10–16]. This method uses the time domain signals from the FMC dataset to systematically focus at each point in the imaging domain, creating an image of the inspection area. However, an element of subjec-

2

tivity is introduced using such empirical imaging techniques as they rely on arbitraily chosen imaging thresholds at which the defect measurements are taken. Previous work has been carried out to address this issue in [24–26], where objective crack length measurements were made using time-frequency domain scattering matrices. In this paper, an objective model based method is presented for tackling the specific problem of sizing cracks within an elastic solid. This method utilises the Kirchhoff scattering model, a high frequency approximation to the scattering of a linear elastic wave from an ellipsoid within a homogeneous medium. By approximating the model scattering matrices by Toeplitz matrices, an expression relating the crack size to the maximum eigenvalue of the associated scattering matrix is derived. The formula is analysed numerically to assess its sensitivity to the system parameters and is finally applied to simulated FMC data arising from finite element calculations.

2   Kirchoff model and scattering matrices

The Kirchhoff model is used to provide a high frequency approximation to the scattering of a linear elastic wave from a crack in a homogeneous medium. The signals scattered from a crack in the host material are represented in the frequency domain by scattering matrices, which are a function of the transmitted and received waves. Figure 1 shows a schematic of the model geometry, where the ellipsoidal crack is lying in the plane $x_1 = 0$ and the ultrasonic waves emanating from the array lie in the plane $x_3 = 0$. An analytical form for the scattering amplitude can be derived by assuming that the flaw is an ellipsoid (with axes lengths a_1, a_2 and a_3 as in Figure 1). To simulate a zero volume flaw (a crack) in the $x_3 = 0$ plane then the ellipsoidal axis a_1 is set equal to zero. The flaw is positioned so that its

centre lies at the origin. An expression for the scattering amplitude of an ellipsoidal crack by a transmitted pressure wave in a homogeneous elastic medium is then given by (equation (10.168), [27])

$$A_n(\mathbf{e}_i, \mathbf{e}_s) = -\frac{ia_2a_3e_{sl}e_{sn}e_{sj}C_{kplj}(e_{ip} - e_{rp})n_k}{2\rho c^2|\mathbf{e}_i - \mathbf{e}_s|r_e}J_1\left(\frac{2\pi}{\lambda}|\mathbf{e}_i - \mathbf{e}_s|r_e\right) \quad (1)$$

where $\mathbf{e}_i$ and $\mathbf{e}_s$ are the unit vectors in the transmitting and receiving direction of the ultrasonic wave. It is important to note that in this paper only pressure waves are considered. The unit vector $\mathbf{e}_r$ is in the direction of the specular reflection from the crack; the specular reflection is in the direction of the maximum amplitude reflected wave. The angle between the specular reflection direction and the normal to the crack is equal to that between the direction of the transmitted wave and the normal, as demonstrated in Figure 2. In addition, c is the wave speed for a pressure wave, ρ is the host material density, λ is the wavelength of the transmitted pressure wave, C_{kplj} is the elastic modulus tensor, J_1 is the Bessel function of the first kind of order 1 and r_e is the effective radius of the crack. In an isotropic, homogeneous medium the elastic modulus tensor in equation (1) reduces to $C_{kplj} = L\delta_{kp}\delta_{lj} + \mu(\delta_{kl}\delta_{pj} + \delta_{kj}\delta_{pl})$, where L and μ are the Lamé co-efficients. Letting $\mathbf{e}_q = (\mathbf{e}_i - \mathbf{e}_s)/|\mathbf{e}_i - \mathbf{e}_s|$ and $\mathbf{u}_2, \mathbf{u}_3$ be unit vectors along the x_2, x_3 axis respectively, then the effective radius of the crack is defined as

$$r_e = \sqrt{a_2^2(\mathbf{e}_q \cdot \mathbf{u}_2)^2 + a_3^2(\mathbf{e}_q \cdot \mathbf{u}_3)^2} = a_2|\mathbf{e}_q \cdot \mathbf{u}_2| \quad (2)$$

since $\mathbf{e}_i$ and $\mathbf{e}_s$ are perpendicular to $\mathbf{u}_3$. By substituting the definition of the elastic modulus tensor and equation (2) into equation (1) it can be written
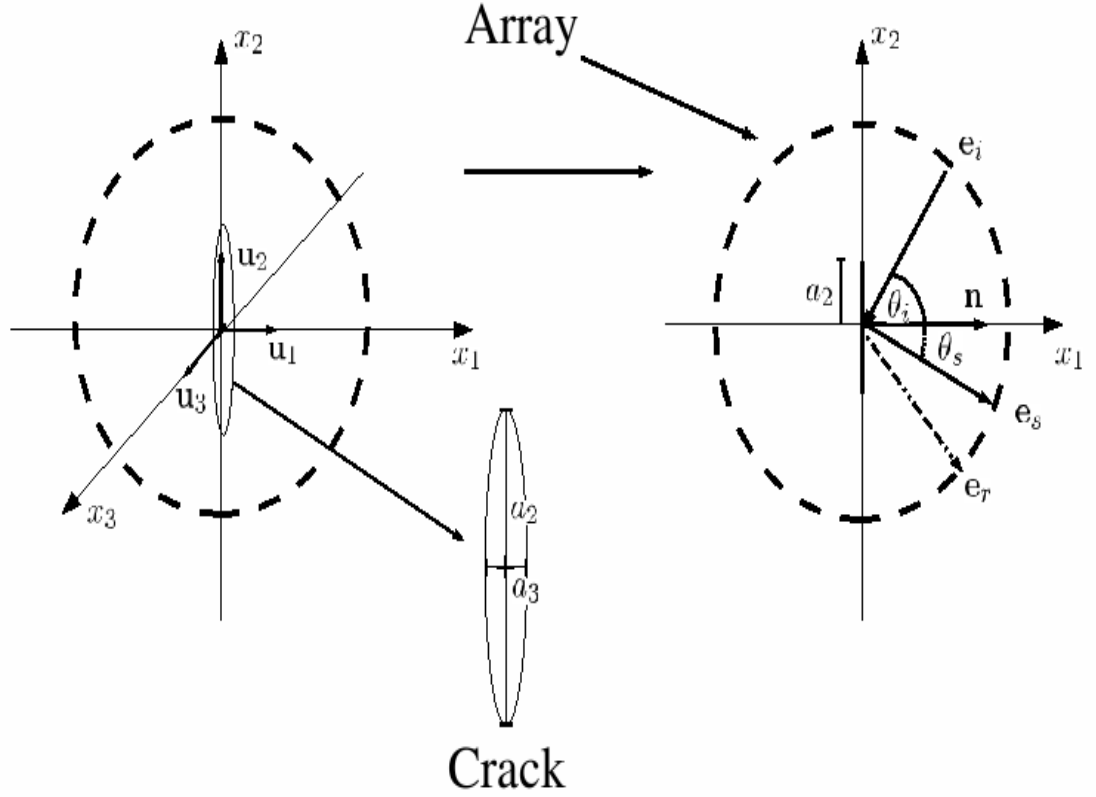
4

Figure 1: A schematic of the geometry used to derive the scattering matrices that arise in the Kirchhoff model (equation (1)) for a crack inclusion in an elastic solid. Here $2a_2$ is the crack length, $\mathbf{n}$ is the normal to the crack, $\mathbf{e}_i$ ($\mathbf{e}_r, \mathbf{e}_s$) is the transmitted (receiving, specular) wave direction, $\theta_i(\theta_s)$ is the angle measured in an anticlockwise direction from the positive x_1 axis of the transmitted (received) wave and $\mathbf{u}_1, \mathbf{u}_2$ and $\mathbf{u}_3$ are unit vectors in the x_1, x_2 and x_3 directions.

that

$$A_n(\mathbf{e}_i; \mathbf{e}_s) = -\frac{ia_3 e_{sn}(L((\mathbf{e}_i - \mathbf{e}_r) \cdot \mathbf{n}) + 2\mu((\mathbf{e}_i - \mathbf{e}_r) \cdot \mathbf{e}_s)(\mathbf{e}_s \cdot \mathbf{n}))}{2\rho c^2 |(\mathbf{e}_i - \mathbf{e}_s) \cdot \mathbf{u}_2|} J_1\left(\frac{2\pi a_2}{\lambda}|(\mathbf{e}_i - \mathbf{e}_s) \cdot \mathbf{u}_2|\right).$$

(3)

where the scale factor a_3 has been dropped and the scattering amplitude

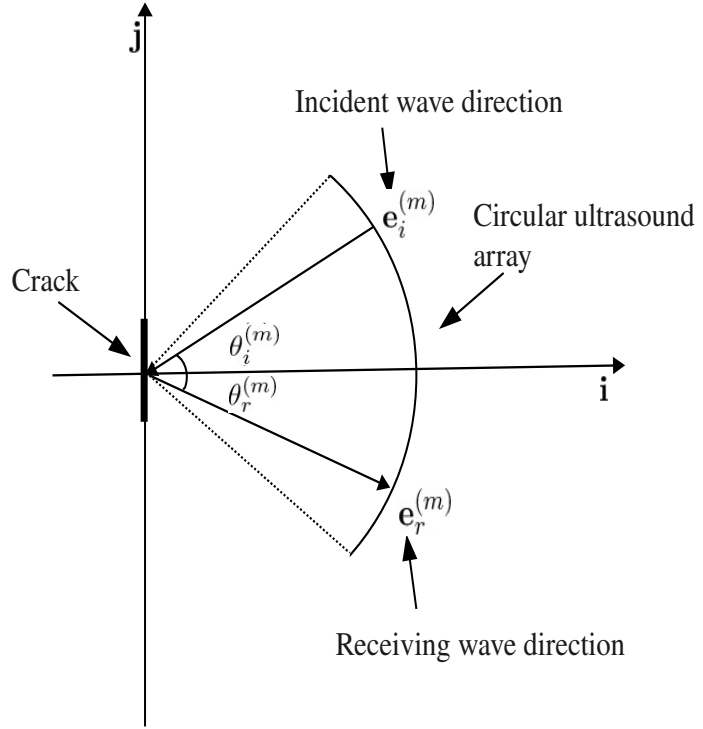has been converted into a scalar value by taking the scalar product with

Figure 2: A schematic showing the location of the unit vector in the specular reflection direction, $\mathbf{e}_r^{(m)}$, with respect to the unit vector in the incident direction, $\mathbf{e}_i^{(m)}$, on a limited aperture, circular array.

the direction of reception, $\mathbf{e}_s$. The transmitted and received wave directions can be defined at a discrete set of values and if these completely surround the flaw it is called a *full aperture*. By calculating the absolute value of the scattering amplitude given in equation (3) for every possible pair of transmitting and receiving angles (at a fixed frequency), a scattering matrix can be constructed, with the largest entries occuring close to the specular reflection.

3 Approximation to a limited aperture ultrasonic array

The Kirchhoff model provides the response from a full aperture, circular array which is shown by the dashed line in Figure 1. However, in this work the circular array is approximated by a discretised linear limited aperture array as this is all that can be measured in practice. The approximation to a limited aperture array allows the expression for the scattering matrices given by equation (3) to be parameterised. The unit vector in the receiving direction for the nth element in the ultrasound array is given by

$$\mathbf{e}_s^{(n)} = \frac{d}{\sqrt{d^2 + q_n^2}}\mathbf{i} + \frac{q_n}{\sqrt{d^2 + q_n^2}}\mathbf{j} = \sqrt{1 - \hat{q}_n^2}\,\mathbf{i} + \hat{q}_n\mathbf{j}. \tag{4}$$

where d is the minimum distance between the flaw and the ultrasound array (it is assumed here that the centre of the array is the closest point in the array to the flaw), q_n dictates the element position,

$$q_n = \frac{\triangle q}{2}(N + 1 - 2n), \tag{5}$$

where N is the total number of elements in the ultrasound array and the periodicity of the array elements (the pitch) is given by

$$\triangle q = \frac{l}{N - 1} \tag{6}$$

where l is the array length (aperture) as shown in Figure 3.

In the analysis below it is assumed that N is even and that the array elements are evenly spaced (that is, the array pitch $\triangle q$ is a constant). The forthcoming analysis is simplified if $\hat{q}_n$ is approximated as a linear function
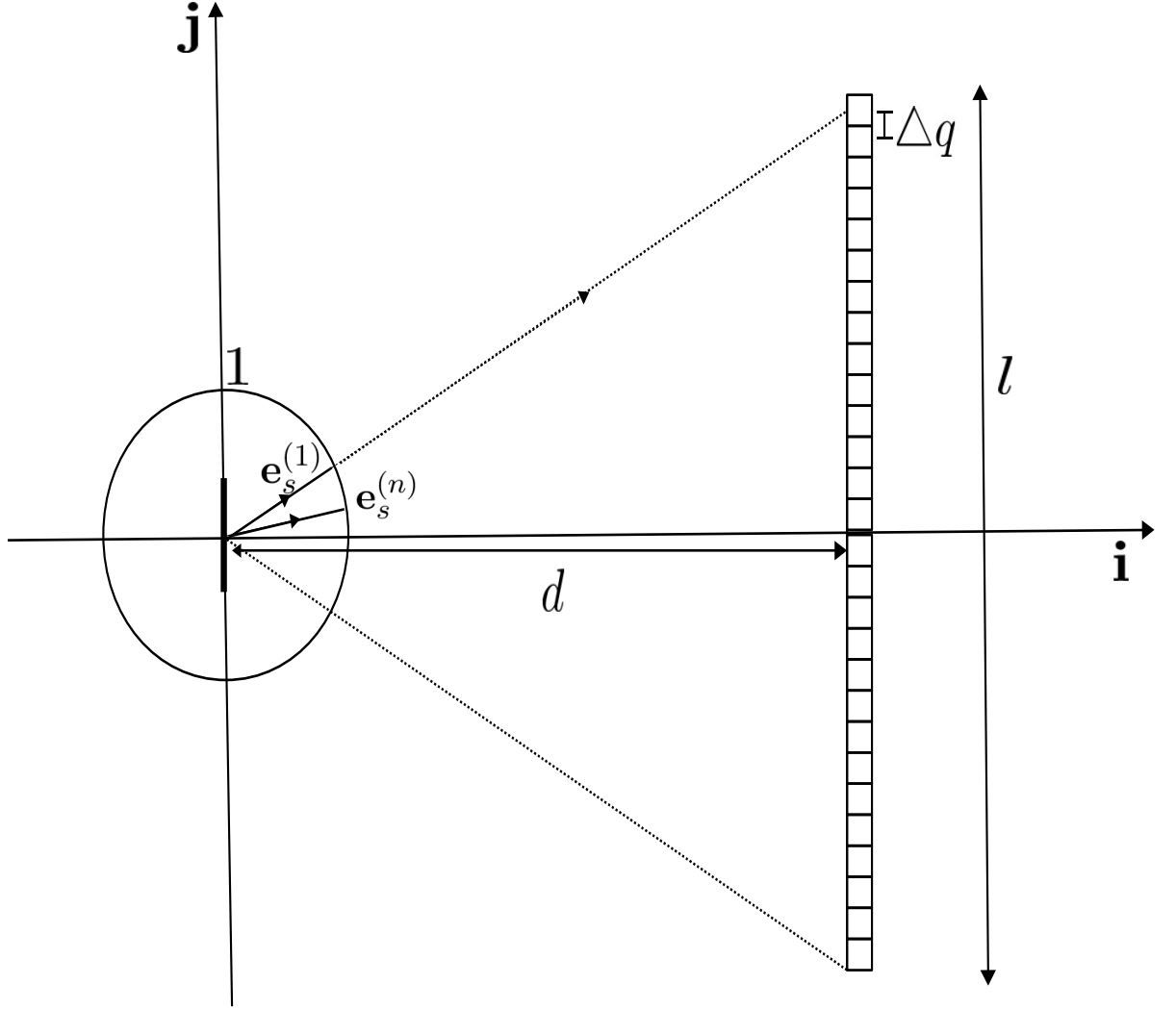
Figure 3: A schematic demonstrating the geometry of the linear ultrasound array. The unit vector $\mathbf{e}_s^{(n)}$ is in the receiving direction for array element n on the array. The array is of length l, the flaw is at a depth d from the array and $\triangle q$ gives the pitch between the array elements.

of n. Combining equations (4), (5) and (6) then

$$\hat{q}_n = \frac{l}{\sqrt{4d^2 + l^2(1 - h(n))^2}} \frac{N + 1 - 2n}{N - 1} \tag{7}$$

where $h(n) = 2(n - 1)/(N - 1)$. The denominator in the expression for $\hat{q}_n$

in equation (7) is manipulated further to give

$$\hat{q}_n = \frac{l}{\sqrt{4d^2 + l^2}} \frac{N+1-2n}{N-1} \frac{1}{\sqrt{1-\alpha}} \tag{8}$$

where $\alpha = l^2(2h - h^2)/(4d^2 + l^2)$. Since $0 \leq h \leq 2$ for $n = 1, ..., N$ then $0 \leq 2h - h^2 \leq 1$, and since $0 < l^2/(4d^2 + l^2) < 1$, then α is small. A Taylor series approximation is applied to equation (8) to approximate $\hat{q}_n$ as

$$\hat{q}_n = y_n + \mathcal{O}(\alpha^2) \tag{9}$$

where

$$y_n = \triangle y(N + 1 - 2n)/2 \tag{10}$$

and

$$\triangle y = \frac{l}{((N-1)\sqrt{4d^2 + l^2})}. \tag{11}$$

From equation (4) the approximate transmitting and receiving unit vectors are therefore given by

$$\mathbf{e}_i^{(m)} = -\sqrt{1 - y_m^2}\mathbf{i} - y_m\mathbf{j}, \qquad m = 1, ..., N \tag{12}$$

and

$$\mathbf{e}_s^{(n)} = \sqrt{1 - y_n^2}\mathbf{i} + y_n\mathbf{j}, \qquad n = 1, ..., N. \tag{13}$$

By restricting attention to the case where the flaw is orientated to lie along the x_2 axis then the specular reflection is given by

$$\mathbf{e}_r^{(m)} = \sqrt{1 - y_m^2}\mathbf{i} - y_m\mathbf{j}, \qquad m = 1, ..., N \tag{14}$$

Since the flaw lies on the x_2 axis (that is $\mathbf{u}_2 = \mathbf{j}$ and $\mathbf{n}=\mathbf{i}$) then equation (3)

9

becomes

$$A(y_m, y_n) = \frac{\sqrt{1 - y_m^2}}{\rho c^2 |y_n + y_m|} (L + 2\mu(1 - y_n^2)) J_1\left(2\pi\hat{a}|y_n + y_m|\right) \doteq \frac{1}{\rho c^2} A_{m,n} \quad (15)$$

where $\hat{a} = a_2/\lambda$ and $2a_2$ is the crack length. In the next section a crack sizing method is developed which relates the maximum eigenvalue of the scattering matrix $A_{m,n}$ to the length of the crack.

4 Crack sizing using the maximum eigenvalue

It is clear from empirical observations that there is a relationship between the size of the crack and the form of the scattering matrix [25]. It would therefore be advantageous if an analytical approach could be developed to capture this correlation. From the scattering matrices in Figure 4 it can be seen that the dominant values aggregate around the skew diagonal. There is a considerable body of research concerning Toeplitz matrices and in an effort to benefit from this body of work the scattering matrix, A (given by equation (15)), will be approximated by a Toeplitz matrix. First, the matrix A is transformed to A_T via

$$A_T(y_{m'}, y_n) = A(y_m, y_n) \qquad \text{where} \qquad m' = N - m + 1 \qquad (16)$$

so that the dominant values accumulate around the main diagonal. The transformed scattering matrix, A_T, will be approximated by a Toeplitz matrix, where the row where the maximum of $A_T(y_m, y_n)$ occurs will be used to create this Toeplitz approximation, $\bar{A}_T$. This row is highlighted by the green squares in the original scattering matrix, A, in Figure 4 (a) and in

10

the transformed matrix, A_T, in Figure 4 (b). The Toeplitz matrix resulting from this matrix is shown in Figure 4 (c) where all remaining entries in the row are filled with zeroes. To begin we observe that in equation (15) the term

$$\frac{J_1\left(2\pi\hat{a}(y_n + y_m)\right)}{y_n + y_m} \tag{17}$$

obtains its maximum when $y_n + y_m = 0$. The prefactor to the Bessel function in equation (15) is given by

$$\sqrt{1 - y_m^2}(L + 2\mu(1 - y_{n'}^2)), \tag{18}$$

and, since $0 < y_m^2, y_n^2 < 1$, this is also maximised when $y_m = y_n = 0$. Since the array is centred on the x_1-axis, this means that $y_m = y_n = 0$ corresponds to the centre of the array. If N is odd then the central element is given by $n = m = (N+1)/2$ and if N is even then the smallest value is $y_m = y_n = -\triangle y/2$ which occurs at $n = m = N/2 + 1$. In what follows the focus will be on the case where N is even (the analysis is virtually identical for the case where N is odd) and so we will take this row of A (and hence A_T) to form our Toeplitz approximation. Substituting $y_m = -\triangle y/2$ into equation (15) gives the first $N/2$ entries in the first row of the Toeplitz matrix $\bar{A}_T$ as

$$\bar{A}_T(y_p) = \frac{2\sqrt{1 - \triangle y^2/4}(L + 2\mu(1 - y_p^2))}{\rho c^2(2y_p - \triangle y)}J_1\left(2\pi\hat{a}\left(y_p - \frac{\triangle y}{2}\right)\right) \tag{19}$$

where $p = N/2 + 1, ..., N$ and the absolute value has been removed as $y_p - \triangle y/2 < 0$ and $J_1(2\pi\hat{a}(y_p - \triangle y/2)) < 0$. This row is highlighted in the scattering matrix shown in Figure 4 (b). The remaining terms in the first row of $\bar{A}_T$ are set equal to zero (that is $(\bar{A}_T)_j = 0, j = N/2 + 1, ..., N$). The approximation of the scattering matrix by a Toeplitz matrix can be justified
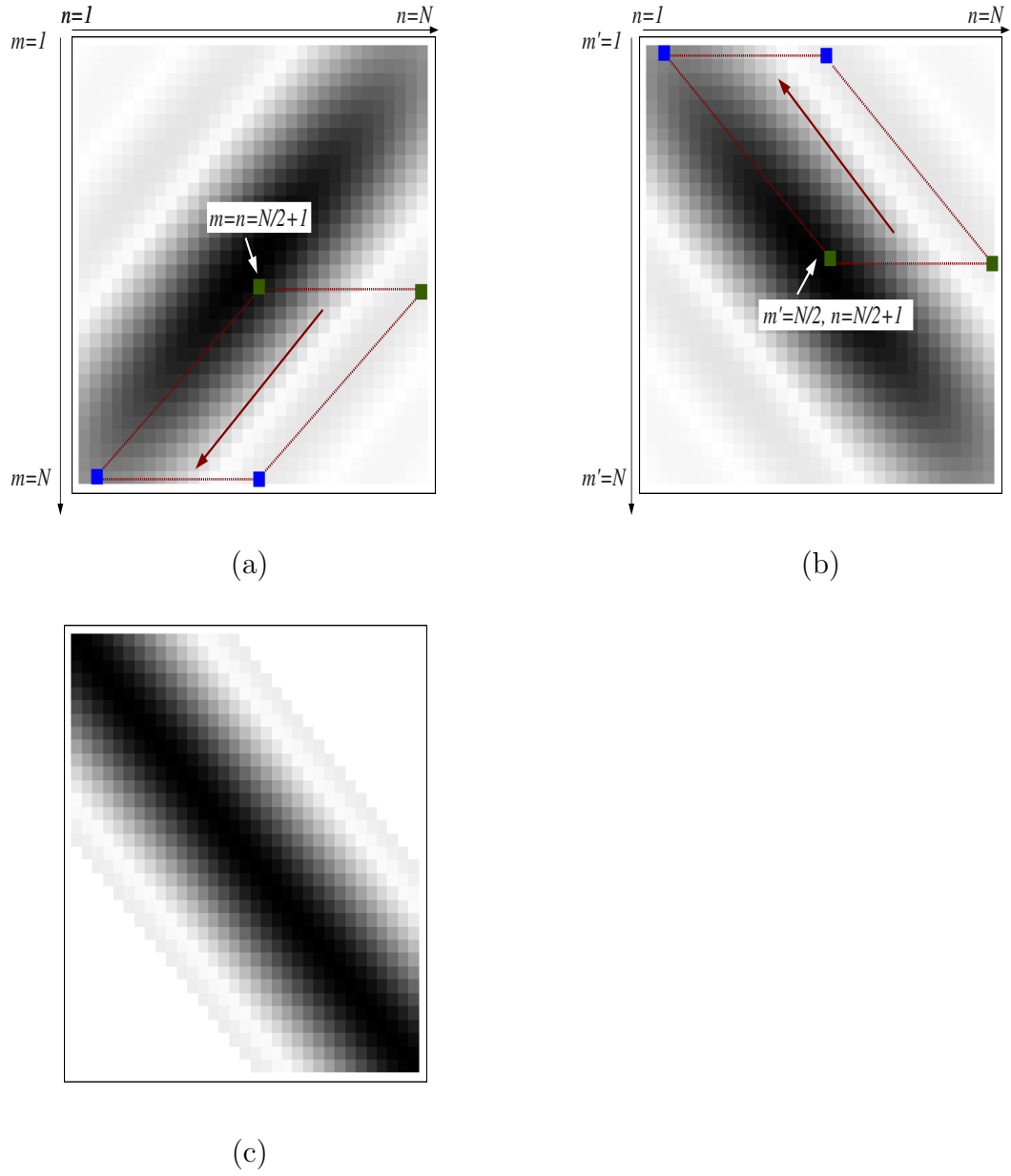
11

(a)

(b)

(c)

Figure 4: The original scattering matrix, A (equation (15), is shown in (a) where the green squares highlight the section of the row which is used to construct the Toeplitz approximation. This is the row where the maximum occurs at $n = m = N/2 + 1$. The red dashed lines highlight the rows which are shown to be approximately equal to the portion of the row where the maximum occurs (shown by the green squares). The equivalent is highlighted in the transformed matrix, A_T (equation (16)), in (b) and (c) shows the Toeplitz matrix, $\bar{A}_T$ (equation (19), constructed using the row where the maximum occurs.

by showing that

$$\left| \frac{A(y_{N/2+1}, y_n) - A(y_m, y_{n-m+N/2+1})}{A(y_{N/2+1}, y_n)} \right| = \mathcal{O}(\epsilon) \qquad \forall m, n = N/2 + 1, ..., N, \tag{20}$$

where $0 < \epsilon \ll 1$ is of the order of the array aperture size squared (typically $\epsilon \sim \mathcal{O}(10^{-2})$) (see Appendix A).

4.1 An approximation for the maximum eigenvalue of the Toeplitz form of the scattering matrix.

In the forthcoming section an approximation which relates the radius of a crack in terms of the wavelength, $\hat{a}$, to the maximum eigenvalue σ_{max} of the Toeplitz approximation to the scattering matrix will be derived. This maximum eigenvalue is approximated using an upper bound, σ_B, which is given by [28]

$$\sigma_B = (\bar{A}_T)_1 \cdot \mathbf{w} \tag{21}$$

where $(\bar{A}_T)_1 = ((\bar{A}_T)_{1,1}, |(\bar{A}_T)_{1,2}|, ..., |(\bar{A}_T)_{1,N}|)$, $\mathbf{w} = (1, w_2, ...w_N)$ and

$$w_k(N) = 2\cos\left(\frac{\pi}{\left\lfloor \frac{N-1}{k-1} \right\rfloor + 2} \right), \tag{22}$$

where $\lfloor . \rfloor$ denotes the *floor* function. The first row of the Toeplitz matrix, $\bar{A}_T(y_p)$, is given by equation (19) and when substituted into equation (21) gives

$$\sigma_B = \bar{A}_T(y_{N/2+1}) + \sum_{t=N/2+2}^{N} |A_T(y_t)| w_t$$

$$= \bar{A}_T(y_{N/2+1}) + \sum_{t=N/2+2}^{N} F_t(\hat{a}) \frac{J_1\left(2\pi\hat{a}\left(y_t - \triangle y/2\right)\right)}{2\pi\hat{a}\left(y_t - \triangle y/2\right)} w_t, \tag{23}$$

13

where

$$w_t(N) = 2\cos\left(\frac{\pi}{\left\lfloor \frac{2(N-1)}{2t-2-N} \right\rfloor + 2}\right), \tag{24}$$

with $k = t - N/2$ and the prefactor is given by

$$F_t(\hat{a}) = \frac{2\pi\hat{a}\sqrt{1-(\triangle y)^2/4}}{\rho c^2}(L + 2\mu(1-y_t^2)). \tag{25}$$

The true (numerically calculated) maximum eigenvalue from a scattering matrix from the Kirchhoff model is plotted as a function of the crack radius over the wavelength ($\hat{a}$) in Figure 5 (blue line). The approximation to this maximum eigenvalue given by equation (23) is also plotted in this figure (green line) and there is good agreement as $\hat{a}$ is varied. In order to view the explicit dependency of σ_B on $\hat{a}$ it is necessary to make approximations to the expression within the summation in equation (23). The Bessel function within equation (23) is approximated by

$$\frac{J_1\left(2\pi\hat{a}\left(y_t - \triangle y/2\right)\right)}{2\pi\hat{a}\left(y_t - \triangle y/2\right)} = \begin{cases} f_t^{(1)}(\hat{a}) & \text{if } N/2 + 2 \leq t \leq t^* \\ \\ f_t^{(2)}(\hat{a}) & \text{if } t^* + 1 \leq t \leq N \end{cases}$$

where the approximation for small arguments [29] is used to obtain

$$f_t^{(1)}(t,\hat{a}) = \overbrace{\frac{1}{2}\left(1 - \frac{1}{4}\left(\pi\hat{a}\left(y_t - \frac{\triangle y}{2}\right)\right)^2\right)}^{\bar{f}_t^{(1)}} + \mathcal{O}\left(\frac{1}{384}\left(\pi\hat{a}\left(y_t - \frac{\triangle y}{2}\right)\right)^4\right) \tag{26}$$

and for large arguments [29]

$$f_t^{(2)}(t,\hat{a}) = \overbrace{\frac{1}{2\pi^2}\left(\hat{a}\left(y_t - \frac{\triangle y}{2}\right)\right)^{-\frac{3}{2}}\cos\left(2\pi\hat{a}\left(y_t - \frac{\triangle y}{2}\right) - \frac{3\pi}{4}\right)}^{\bar{f}_t^{(2)}} \tag{27}$$

$$+ \mathcal{O}\left(\frac{3}{24\pi^3}\sin\left(\hat{a}\left(y_t - \frac{\triangle y}{2}\right) - \frac{3\pi}{4}\right)\left(\hat{a}\left(y_t - \frac{\triangle y}{2}\right)\right)^{-\frac{5}{2}}\right).$$

14

The index t^* determines when the argument of the Bessel function converts from small values to large values. An expression for t^* can be determined (see Appendix B) and is given in terms of the system parameters and $\hat{a}$. Evaluating equation (19) at $p = N/2 + 1$ gives

$$\bar{A}_T(y_{N/2+1}) = \bar{A}_T\left(-\frac{\triangle y}{2}\right) = F_{N/2+1}(\hat{a}) = \frac{2\hat{a}\pi\sqrt{1 - (\triangle y)^2/4}\left(L + 2\mu\left(1 - (\triangle y)^2/4\right)\right)}{\rho c^2}$$

(28)

where $0 < \triangle y \ll 1$. The approximation to equation (23) is split into two summations and is therefore given by

$$\sigma_B = F_{N/2+1}(\hat{a}) + \sum_{t=N/2+1}^{t^*} F_t(\hat{a})\bar{f}_t^{(1)}(\hat{a})w_t(N) + \sum_{t=t^*+1}^{N} F_t(\hat{a})\bar{f}_t^{(2)}(\hat{a})w_t(N)$$

$$+ \mathcal{O}\left(\max\{e_1, e_2\}\right)$$

(29)

where

$$e_1 = \frac{\pi^4\hat{a}^4}{384}\sum_{t=N/2+1}^{t^*}\left(y_t - \frac{\triangle y}{2}\right)^4 w_t(N)F_t(\hat{a})$$

(30)

and

$$e_2 = \frac{3}{24\pi^3}\sum_{t=t^*+1}^{N}\left(\hat{a}\left(y_t - \frac{\triangle y}{2}\right)\right)^{-\frac{5}{2}}\sin\left(2\pi\hat{a}\left(y_t - \frac{\triangle y}{2}\right) - \frac{3\pi}{4}\right)F_t(\hat{a})w_t(N).$$

(31)

As these error functions are monotonically increasing in t then, by taking $t = t^*$ for all t upper bounds can be derived (see Appendix B). Further approximations are applied to equation (27) to allow σ_B to be expressed in terms of a polynomial in t. This will be useful later where the aim is to extract the parameter $\hat{a}$ in order to obtain an explicit expression which relates σ_B to $\hat{a}$. Let

$$\bar{f}_t^{(2)}(\hat{a}) = s_t^{(1)}(\hat{a})s_t^{(2)}(\hat{a})$$

(32)

15

where

$$s_t^{(1)}(t, \hat{a}) = \frac{1}{\pi^2} \left(\frac{2}{\hat{a}\triangle y(N - 2t)} \right)^{\frac{3}{2}}, \tag{33}$$

and

$$s_t^{(2)}(\hat{a}) = \cos\left(\pi\hat{a}\triangle y(N - 2t) - \frac{3\pi}{4} \right). \tag{34}$$

The Taylor series approximation of s_1 around the point $t = m = (t^* + N)/2$ (the midpoint between t^* and N) is given by

$$s_t^{(1)}(\hat{a}, m) = \overbrace{\frac{1}{2\pi^2} \left(\frac{1}{\hat{a}\triangle y(N - 2m)} \right)^{3/2} \left(1 + \frac{3}{N - 2m}(t - m) \right)}^{\bar{s}_t^{(1)}}$$
$$+ \mathcal{O}\left(15\hat{a}^2(\triangle y)^2 \left(\frac{1}{\hat{a}\triangle y(N - 2m)} \right)^{7/2} (t - m)^2 \right). \tag{35}$$

and similarly

$$s_t^{(2)}(\hat{a}, m) = \cos\left(\pi\hat{a}\triangle y(N - 2t) - \frac{3\pi}{4} \right) \left(1 - 2\left(\hat{a}\pi\triangle y(t - m) \right)^2 \right)$$
$$+ \sin\left(\pi\hat{a}\triangle y(N - 2t) - \frac{3\pi}{4} \right) \left(-2\hat{a}\pi\triangle y(t - m) + \frac{4}{3}\left(\hat{a}\pi\triangle y(t - m) \right)^3 \right)$$
$$+ \mathcal{O}\left(\frac{2}{3}(\pi\hat{a}\triangle y)^4 (t - m)^4 \cos\left(\pi\hat{a}\triangle y(N - 2t) - \frac{3\pi}{4} \right) \right)$$
$$= \bar{s}_t^{(2)} + \mathcal{O}\left(\frac{2}{3}(\pi\hat{a}\triangle y)^4 (t - m)^4 \cos\left(\pi\hat{a}\triangle y(N - 2t) - \frac{3\pi}{4} \right) \right). \tag{36}$$

This gives the approximation

$$\bar{f}_t^{(2)}(\hat{a}, m) = \bar{s}_t^{(1)}\bar{s}_t^{(2)} + \mathcal{O}(\max\{e_3, e_4\}) \tag{37}$$

16

where

$$e_3 = \mathcal{O}\left(\bar{s}_t^{(2)}(\hat{a}, m)F_t(\hat{a})w_t(N)15\hat{a}^2(\triangle y)^2\left(\frac{1}{\hat{a}\triangle y(N-2m)}\right)^{7/2}(t-m)^2\right)$$

(38)

and

$$e_4 = \mathcal{O}\left(\bar{s}_t^{(1)}(\hat{a}, m)F_t(\hat{a})w_t(N)\frac{2}{3}(\pi\hat{a}\triangle y)^4(t-m)^4\cos\left(\pi\hat{a}\triangle y(N-2t)-\frac{3\pi}{4}\right)\right).$$

(39)

Substituting equations (35) and (36) into equation (29) gives

$$\sigma_B = F_{N/2+1}(\hat{a}) + \sum_{t=p+1}^{t^*}\left[F_t(\hat{a})\bar{f}_t^{(1)}w_t(N)\right]$$

$$+ \sum_{t=t^*}^{N}\left[F_t(\hat{a})\bar{s}_t^{(1)}(t, \hat{a}, m)\bar{s}_t^{(2)}(t, \hat{a}, m)w_t(N)\right] + \mathcal{O}\left(\max\{e_1, e_2, e_3, e_4\}\right).$$

(40)

Finally, w_t given by equation (24) is approximated by a linear function. First the *floor* function within the cosine in equation (22) is dropped (a justification is given in Appendix C) to give

$$w_t = 2\cos\left(\frac{\pi}{\frac{2(N-1)}{2t-N-2}+2}\right)$$

$$= 2\cos\left(\frac{\pi(2t-2-N)}{2(2t-3)}\right).$$

(41)

17

The function is then approximated by a Taylor series about $3N/4$ (the midpoint in the range $t = N/2 + 1$ to $t = N$) to give

$$
w_t(N) = \overbrace{2\cos\left(\frac{\pi(N-4)}{6(N-2)}\right) - \frac{8\pi(N-1)\,(t-3N/4)}{9(N-2)^2}\sin\left(\frac{\pi(N-4)}{6(N-2)}\right)}^{\bar{w}_t(N)}
$$
$$
+ \mathcal{O}\left(2\left(t-\frac{3N}{4}\right)^2\left(\frac{8\pi(N-1)}{27(N-2)^3}\right)\left(2\sin\left(\frac{\pi(N-4)}{6(N-2)}\right)\right.\right.
$$
$$
\left.\left.- \frac{\pi^2(N-1)}{3(N-2)}\cos\left(\frac{\pi(N-4)}{6(N-2)}\right)\right)\right).
\tag{42}
$$

This is substituted into equation (40) to give

$$
\sigma_B = F_{N/2+1}(\hat{a})
$$
$$
+ \sum_{t=N/2+2}^{t^*} F_t(\hat{a})\bar{f}_t^{(1)}\bar{w}_t(N)
$$
$$
+ \sum_{t=t^*}^{N} F_t(\hat{a})\bar{s}_t^{(1)}(\hat{a},m)\bar{s}_t^{(2)}(\hat{a},m)\bar{w}_t(N)
$$
$$
+ \mathcal{O}\left(\max\{e_1, e_2, e_3, e_4, e_5, e_6\}\right)
\tag{43}
$$

where

$$
e_5 = \mathcal{O}\left(2\left(t-\frac{3N}{4}\right)^2\left(\frac{8\pi(N-1)}{27(N-2)^3}\right)\left(2\sin\left(\frac{\pi(N-4)}{6(N-2)}\right)\right.\right.
$$
$$
\left.- \frac{\pi^2(N-1)}{3(N-2)}\cos\left(\frac{\pi(N-4)}{6(N-2)}\right)\right)
$$
$$
\left.\times \bar{s}_t^{(1)}(\hat{a},m)F_t(\hat{a})\bar{s}_t^{(2)}(\hat{a},m)(N-t)\right)
\tag{44}
$$

and

$$e_6 = \mathcal{O}\left(2\left(t - \frac{3N}{4}\right)^2 \left(\frac{8\pi(N-1)}{27(N-2)^3}\right)\left(2\sin\left(\frac{\pi(N-4)}{6(N-2)}\right)\right.\right.$$
$$\left.- \frac{\pi^2(N-1)}{3(N-2)}\cos\left(\frac{\pi(N-4)}{6(N-2)}\right)\right)$$
$$\left.\times \bar{f}_t^{(1)}(\hat{a})F_t(\hat{a})(t - N/2)\right) \tag{45}$$

The expressions within each summation are polynomials in t which allows σ_B to be expressed in the following form

$$\sigma_B = \hat{A}\hat{a} + \sum_{l=1}^{6} S_l^{(1)}(\hat{a})b_l(\hat{a}) + \sum_{l=1}^{8} S_l^{(2)}(\hat{a})d_l(\hat{a}) \tag{46}$$

where
$$\hat{A} = \frac{\pi\sqrt{1 - \triangle y^2/4})(L + 2\mu\left(1 - \triangle y^2/4\right))}{\rho c^2}, \tag{47}$$

$$S_l^{(1)}(\hat{a}) = \sum_{t=N/2+2}^{t^*} t^{l-1}, \qquad S_l^{(2)}(\hat{a}) = \sum_{t=t^*+1}^{N} t^{l-1}, \tag{48}$$

and b_l and d_l are functions of $\hat{a}$. Since t^* is a function of $\hat{a}$ then to derive an equation where the dependency on $\hat{a}$ is explicit, it is necessary to rewrite these summations so that t^* does not appear as a limit. Using a closed form expression for the sum to n terms of t^p [30] then

$$S_l^{(1)}(\hat{a}) = \frac{(t^*+1)^l}{l} + \sum_{k=1}^{l} \frac{B_k}{l-k}\binom{l-1}{k}(t^*+1)^{l-k} - \frac{(N/2+2)^l}{l}$$
$$- \sum_{k=1}^{l} \frac{B_k}{l-k}\binom{l-1}{k}\left(\frac{N}{2}+2\right)^{l-k} \tag{49}$$

and

$$S_l^{(2)}(\hat{a}) = \frac{(N+1)^l}{l} + \sum_{k=1}^{l} \frac{B_k}{l-k} \binom{l-1}{k} (N+1)^{l-k} - \frac{(t^*+1)^l}{l}$$

$$-\sum_{k=1}^{l} \frac{B_k}{l-k} \binom{l-1}{k} (t^*+1)^{l-k} \tag{50}$$

where B_k is the kth Bernoulli number. The coefficients b_l are expressed in terms of a polynomial function in $\hat{a}$ as follows

$$b_l(\hat{a}) = b_l^{(1)} \hat{a} + b_l^{(2)} \hat{a}^3 \tag{51}$$

where $b_l^{(1)}$ and $b_l^{(2)}$ are functions of the number of elements in the array, N, $\triangle y$, Lamé coefficients L and μ, wave speed c and material density ρ. The dependency on $\hat{a}$ is extracted from the first summation in equation (46) to give

$$\sum_{l=1}^{6} S_l^{(1)}(\hat{a}) b_l(\hat{a}) = \sum_{l=1}^{6} S_l^{(1)}(\hat{a})(b_l^{(1)} \hat{a} + b_l^{(2)} \hat{a}^3)$$

$$= \hat{a} \hat{S}_1(\hat{a}) + \hat{a}^3 \hat{S}_2(\hat{a}) \tag{52}$$

where

$$\hat{S}_1(\hat{a}) = \sum_{l=1}^{6} S_l^{(1)}(\hat{a}) b_l^{(1)} \qquad \text{and} \qquad \hat{S}_2(\hat{a}) = \sum_{l=1}^{6} S_l^{(1)}(\hat{a}) b_l^{(2)}. \tag{53}$$

The coefficients d_l are extracted from equation (40) and are of the form

$$d_l(\hat{a}) \;\; = B(\hat{a})\Bigg(((d_l^{(0)} + d_l^{(1)} \hat{a} + d_l^{(2)} \hat{a}^2 + d_l^{(3)} \hat{a}^3 + d_l^{(4)} \hat{a}^4) \cos(p(\hat{a}))$$

$$+ (d_l^{(5)} + d_l^{(6)} \hat{a} + d_l^{(7)} \hat{a}^2 + d_l^{(8)} \hat{a}^3 + d_l^{(9)} \hat{a}^4) \sin(p(\hat{a}))\Bigg) \tag{54}$$

20

where

$$B(\hat{a}) = \left(\frac{1}{\pi \hat{a} \triangle y (2N - 2t^* - 3)} \right)^{5/2},$$ (55)

and

$$p(\hat{a}) = \frac{\pi}{4} + \hat{a} \pi \triangle y t^*.$$ (56)

The second summation in the expression for σ_B, equation (46), can now be expressed in the form

$$\sum_{l=1}^{8} S_l^{(2)}(\hat{a}) d_l(\hat{a}) = B \sum_{l=1}^{8} S_l^{(2)}(\hat{a}) \Big((d_l^{(0)} + \hat{a} d_l^{(1)} + \hat{a}^2 d_l^{(2)} + \hat{a}^3 d_l^{(3)} + \hat{a}^4 d_l^{(4)}) \cos(p(\hat{a}))$$
$$+ (d_l^{(5)} + \hat{a} d_l^{(6)} + \hat{a}^2 d_l^{(7)} + \hat{a}^3 d_l^{(8)} + \hat{a}^4 d_l^{(9)}) \sin(p(\hat{a})) \Big)$$
$$= \hat{S}_3(\hat{a}) \cos(p(\hat{a})) + \hat{S}_4(\hat{a}) \sin(p(\hat{a}))$$ (57)

with

$$\hat{S}_3(\hat{a}) = B(\hat{a})(D_0 + D_1 \hat{a} + D_2 \hat{a}^2 + D_3 \hat{a}^3 + D_4 \hat{a}^4)$$
$$= B(\hat{a}) \sum_{k=0}^{4} D_k(\hat{a}) \hat{a}^k$$ (58)

and

$$\hat{S}_4(\hat{a}) = B(\hat{a})(D_5 + D_6 \hat{a} + D_7 \hat{a}^2 + D_8 \hat{a}^3 + D_9 \hat{a}^4)$$
$$= B(\hat{a}) \sum_{k=5}^{9} D_k(\hat{a}) \hat{a}^{k-5}$$ (59)

where
$$D_j(\hat{a}) = \sum_{l=1}^{8} S_l^{(2)}(\hat{a}) d_l^{(j)}.$$ (60)

The terms $d_l^{(i)}$ where $i = 1, .., 10$ and $l = 1, .., 6$ are independent of $\hat{a}$ and again are functions of the system parameters. The expression in equation

21

(57) can then be expressed in the form

$$\sum_{l=1}^{8} S_l^{(2)}(\hat{a}) d_l(\hat{a}) = Q(\hat{a}) \cos(p(\hat{a}) - \phi(\hat{a})) \tag{61}$$

where

$$\phi(\hat{a}) = \tan^{-1}\left(\frac{\hat{S}_4(\hat{a})}{\hat{S}_3(\hat{a})}\right) \tag{62}$$

and

$$Q(\hat{a}) = \sqrt{\hat{S}_3(\hat{a})^2 + \hat{S}_4(\hat{a})^2}. \tag{63}$$

Finally, the approximation to the maximum eigenvalue, σ_B, from the scattering matrix, A, defined by equation (15) is

$$\sigma_B(\hat{a}) = (\hat{A} + \hat{S}_1(\hat{a}))\hat{a} + \hat{S}_2(\hat{a})\hat{a}^3 + Q(\hat{a}) \cos(p(\hat{a}) - \phi(\hat{a}))$$
$$+ \mathcal{O}\left(\max\{e_1, e_2, e_3, e_4, e_5, e_6\}\right) \tag{64}$$

after equations (52) and (61) are substituted into equation (46). If $t^* > N$ then $\sigma_B(\hat{a})$ is further reduced to give

$$\sigma_B(\hat{a}) = (\hat{A}_1 + \hat{S}_1(\hat{a}))\hat{a} + \hat{S}_2(\hat{a})\hat{a}^3 + \mathcal{O}\left(\max\{e_1, e_6\}\right) \tag{65}$$

using only equation (52). The final approximation for σ_B given by equation (64) is shown in Figure 5 (red line). This again shows good agreement with the true (numerically calculated from equation (15)) eigenvalue from the Kirchhoff model (blue line).
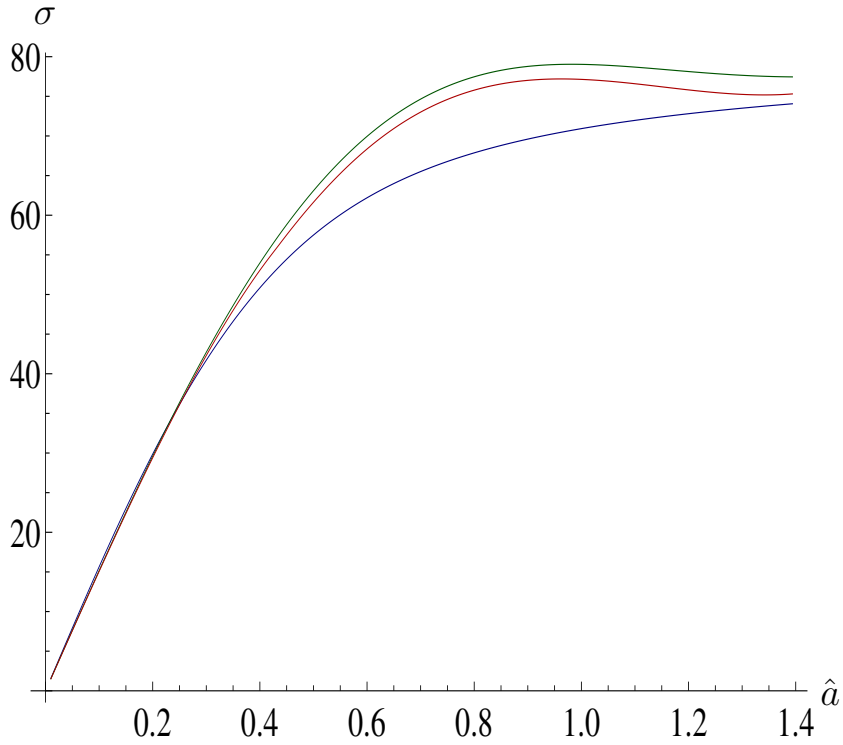
Figure 5: The maximum eigenvalue as a function of $\hat{a}$ from the scattering matrices given by equation (15) (Blue line), the upper bound to the maximum eigenvalue from the Toeplitz approximation to a scattering matrix given by equation (23) (Green line) and the final approximation derived from equation to the maximum eigenvalue given by equation (64) (Red line).

5   The effects of varying the system parameters on the maximum eigenvalue

In order to assess the robustness of this approximation, a comparison with the numerically calculated maximum eigenvalue from the original scattering matrix (given by equation (15)) is made, as the system parameters are varied. In this section each of the system parameters (N, the number of array elements, d, the depth of the flaw, and l, the length of the array) are varied in turn. The effects observed are explained by investigating the changes in the scattering matrices and how these affect the Toeplitz approximation.

5.1 Varying the depth of the flaw, d

As the scattered wave propagates through the material it is attenuated and so, in order to discount this effect, we calculate the scattered field by multiplying the scattered amplitude (given by equation (15)) by $\exp(ikr_m)/r_m$ where $r_m = \sqrt{q_m^2 + d^2}$ and q_m is given by equation (5). Since $d \approx_m$ then this scaling factor can be approximated by $1/\sqrt{2}d$. The maximum eigenvalues
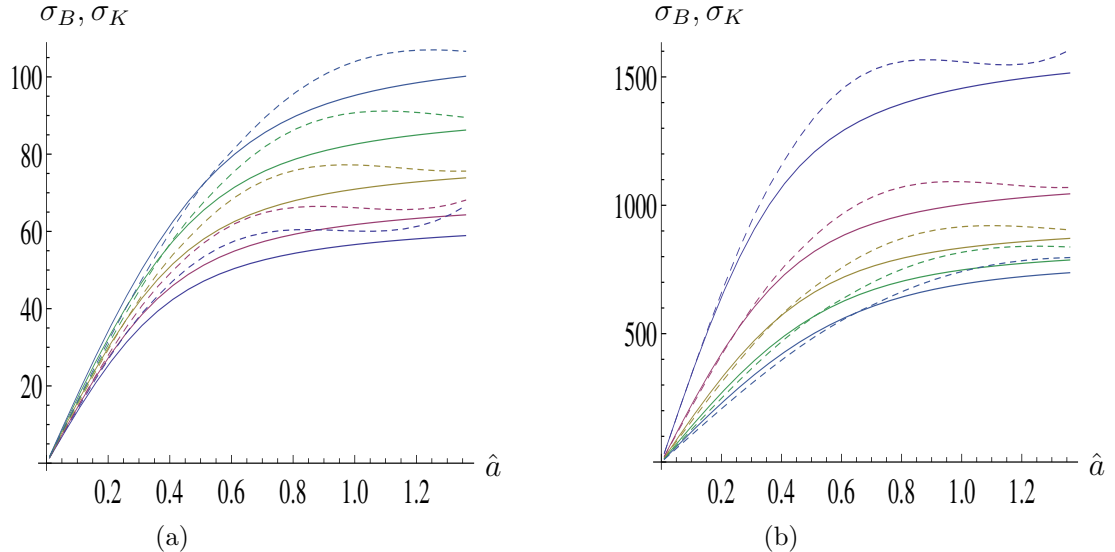

Figure 6: These plots show the approximation to the largest eigenvalue from a scattering matrix, σ_B (dashed lines), equation (64), and the numerically calculated eigenvalue from the scattering matrix, σ_K (solid lines), equation (15), as the crack radius over wavelength, $\hat{a}$, is varied (in both cases a prefactor to account for loss of amplitude with depth $1/\sqrt{2}d$ is used). Each different coloured pair of lines show this comparison for increasing depths of crack from the array; the flaw depth d is 30mm (purple), 50mm (red), 70mm (yellow), 90mm (green) and 110mm (blue). The other system parameters are fixed with the number of array elements, $N = 64$ and the array aperture, $l = 128$mm.

from the scattering matrices from the approximation, σ_B, (dashed lines) in equation (64) and those calculated numerically (solid lines), σ_K, from the model given by equation (15) are plotted in Figure 6 as $\hat{a}$ varies. This figure shows the effects of varying the flaw depth for $d = 30, 50, 70, 90, 110$ (mm).

It can be observed that there is good agreement throughout and that the values of σ_B and σ_K decrease as d increases, which is physically intuitive.

5.2 Varying the number of elements, N

Now the effect of varying the number of elements in the ultrasonic, linear array on the maximum eigenvalue is examined. In this subsection the other system parameters are fixed with $d = 50$mm and $l = 128$mm. Figure 7 shows the plot of the maximum eigenvalue from the approximation σ_B, equation (64), (dashed line) and the mnumerically calculated maximum eigenvalue from the scattering matrices σ_K (solid line) as $\hat{a}$ is varied for $N= 32$ (blue), 64 (red), 128 (yellow) and 256 (green) array elements. This figure shows
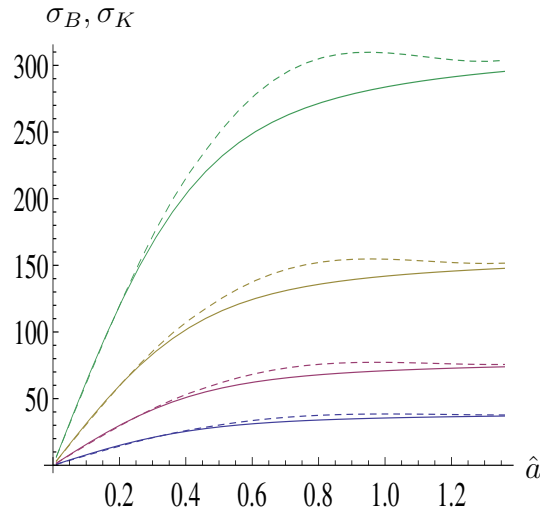

Figure 7: These plots demonstrate the effect of varying the number of elements, N, on the maximum eigenvalue, σ_B. The approximation to the largest eigenvalue (dashed lines), equation (64), and the numerically calculated eigenvalue from the scattering matrix (solid lines), equation (15), are plotted in (a) as a function of the crack radius over the wavelength $\hat{a}$ for various numbers of array elements ($N= 32$ (blue), 64 (red), 128 (yellow), 256 (green)), with $l = 128$mm and $d = 50$mm.

that the maximum eigenvalue from the scattering matrix increases as the number of elements increases in an array of fixed length. In other words, σ_B

is more sensitive ($\partial \sigma_B / \partial \hat{a}$ increases) to the size of the crack as the density of the array elements increases. This is to be expected as the increase in the number of array elements enables more information to be recorded by the ultrasonic transducer and therefore a higher volume of detail is contained within the scattering matrix.

5.3 Varying the array length, l

Increasing the array length has the same effect as decreasing the depth of the flaw. That is, the total angle the array makes with the crack (the array aperture angle) increases as the length of the array increases. As the length
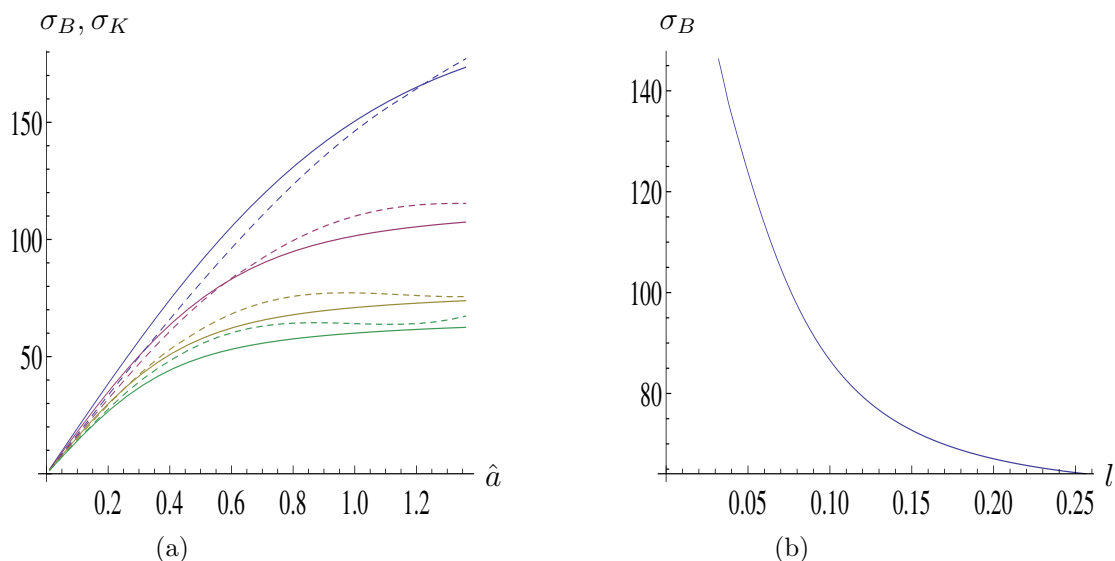

Figure 8: These plots demonstrate the effect of varying the length of the array, l, on the maximum eigenvalue, σ_B. The approximation to the largest eigenvalue (dashed lines), equation (64), and the numerically calculated eigenvalue from the scattering matrix (solid lines), equation (15), are plotted in (a) as a function of the crack radius over the wavelength $\hat{a}$ for various array lengths (l= 32mm (blue), 64mm (red), 128mm (yellow), 256mm (green)), with $N = 64$ and $d = 50$mm. The plot in (b) shows σ_B as l is varied where $\hat{a} = 1$, $N = 64$ and $d = 50$mm.

of the array is increased the maximum eigenvalue, σ_B (dashed lines), from equation (64) and the actual maximum eigenvalue, σ_K (solid lines), decrease as is shown in Figure 8 where σ_B and σ_K are plotted as a function of $\hat{a}$ for various lengths of array (l=32mm (blue), 64mm (red), 128mm (yellow) and 256mm (green)). This seems counterintuitive, however, as the array length is increased (and the array aperture angle is increased) then there is a larger range of values in the scattering matrix; since more of the main lobe in the scattering matrix is captured. This in turn leads to broader spread of eigenvalues and, with less energy being associated with the largest eigenvalue, its value comes down in magnitude. Note also that here the number of array elements, N, is fixed and so the information recorded by the ultrasonic transducer is more sparse. In the next subsection the array length is varied but with the pitch, $\triangle y$, fixed and so the number of array elements, N, and the array length, l, increase proportionally.

5.4   Varying the array length, l, and the number of elements, N

In this subsection the length of the array is varied, however the pitch, $\triangle y$ is fixed; this means that the number of elements in the array is a function of the array length and is given by

$$N = \frac{2l}{\triangle y\sqrt{4d^2 + l^2}} + 1. \tag{66}$$

In this section $\triangle y = 0.025$ and $d = 50$mm. Figure 9 shows the approximation to the maximum eigenvalue σ_B (dashed line) and the numerically calculated maximum eigenvalue σ_K (solid line) as $\hat{a}$ is varied. This figure shows that the maximum eigenvalue now increases as the length of the array (and hence the number of elements and so the array aperture) are increased.

27

This suggests that in experimental investigations one should try and retain a constant pitch when scanning different test peieces (this of course would naturally occur if one uses the same transducer array probe).
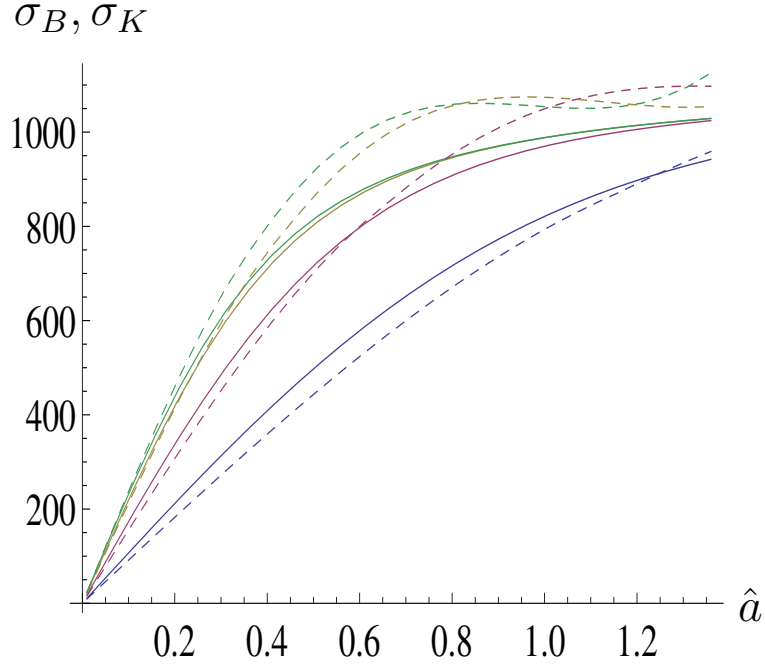
σ_B, σ_K

Figure 9: This plot demonstrates the effect of varying the number of elements, N, and the length of the array l simultaneously on the maximum eigenvalue, σ_B. The approximation to the largest eigenvalue (dashed lines), equation (64), and the numerically calculated eigenvalue from the scattering matrix (solid lines), equation (15), are plotted in (a) as a function of the crack radius over the wavelength $\hat{a}$ for various numbers of array lengths (l= 32mm (blue), 64mm (red), 128mm (yellow), 256mm (green)), with corresponding N ={25, 44, 64, 76} (to the nearest whole number) and the depth of the flaw fixed at $d = 50$mm. The plot in (b) shows σ_B as N is varied where $\hat{a} = 1$ and $d = 50$mm.

This investigation into the effects of the system parameters can lead to other recommendations for experimental designs. For instance, Figure 9 shows that there is very little increase in sensitivity of σ_B to $\hat{a}$ when the array length is increased from 128mm to 256mm (and the number of elements is increased from 64 to 76 since the pitch is fixed at 2mm here). This suggests that if this method is going to be used to resolve the size of

28

a sub-wavelength crack within this medium then it is unnecessary to use an array larger than 128mm, for a fixed pitch of 2.5mm. The sensitivity of the maximum eigenvalue to the system parameters can also be studied analytically by calculating various partial derivatives of the eigenvalue σ_B with respect to these parameters (see Appendix D). This work shows that σ_B is sensitive in particular to changes in the crack radius to wavelength ratio $\hat{a}$ and hence suggests that the inverse problem of recovering $\hat{a}$ from measured values of the maximum eigenvalue should be viable. Importantly, the analysis shows that small errors in the length of the array, l, the number of elements, N and the depth of the flaw, d do not create large errors in σ_B. It was also found that σ_B is particularly sensitive to changes in the crack radius over the wavelength, $\hat{a}$, when $\hat{a} < 0.8$, which implies that this method should be used for sizing cracks commensurate with the wavelength (or at least in that neighbourhood) and for $\hat{a} > 0.8$ another method, such as an image-based method (TFM for example) should be used.

6   Results from simulated data

In this section the method is applied to simulated FMC data in the time domain generated using the finite element package PZFlex [31]. It simulates a crack of length 5mm ($a = 2.5$mm and $\hat{a} \approx 0.5$) within a homogeneous medium, and the parameters used in this simulation are given in Table 1. Each transmit-receive time domain signal was transformed into the frequency domain using a Fast Fourier Transform. A 1.5 MHz single cycle sinusoid wave was used in the simulation and so a $-3dB$ window is taken around this central frequency to give a usable bandwidth of $0.75 - 2.25$MHz (this gives of a range of 0.6 to 1.8 for the crack length to wavelength ratio). The simulation includes a number of effects which are not taken into account in

29

Ultrasonic Transducer Array Parameters	Value	Units
Number of elements	64	-
Pitch	2	mm
Element width	1.5	mm
Transducer centre frequency	1.5	MHz
Array Length	128	mm
Wave speed in host material	6600	ms^{-1}
Density of host material	8280	$\mathrm{kq/m}^3$
Flaw length	5	mm
Depth of flaw	50	mm
Depth of sample	78.6	mm
Time sample rate	173	ns

Table 1: Parameters used in the finite element simulations of a homogeneous medium with a horizontal crack inclusion.

the Kirchhoff model used in this work. For example, in the Kirchhoff model (as used here) there is no mode conversion of the wave considered when it encounters the crack; only a pressure wave is considered. This results in amplitude differences between the scattering matrices from the simulated data and the model and therefore the scattering matrices need to be normalised. The scattering matrices from the simulated data, $A_S(m, n, f)$, and from the model, $A_K(m, n, a, f)$, (where $m, n = 1, ..., N$ correspond to transmitting and receiving element indices) are normalised with respect to the l^2-norm to allow the signatures of each to be compared as crack radius, a, and frequency, f are varied. That is, for the simulated data let

$$\bar{A}_S(m, n) = \frac{A_S(m, n, f)}{\sqrt{\sum_{m=1}^{N} \sum_{n=1}^{N} A_S(m, n, f)^2}} \qquad (67)$$

and similarly from the Kirchhoff model (equation (15)) the normalised scattering matrix is

$$\bar{A}_K(m, n) = \frac{A_K(m, n, a, f)}{\sqrt{\sum_{m=1}^{N} \sum_{n=1}^{N} A_K(m, n, a, f)^2}}. \qquad (68)$$

Let $\sigma_S(f)$ denote the numerically calculated maximum eigenvalue from the normalised scattering matrix, given by equation (67), at a fixed frequency, f, and let $\sigma_K(a, f)$ denote the numerically calculated maximum eigenvalue from the Kirchhoff model (equation (68)) at a frequency f and for a crack of radius a. Figure 10 shows the plot of σ_S (blue line) across the frequency range $0.75 - 2.25$MHz and compares this with σ_K from the model for the same range of frequencies for different values of crack radii. This figure shows that $\sigma_K(a, f)$ is sensitive to changes in crack radius (as our analysis showed) and that $\sigma_S(f)$ compares well with $\sigma_K(a, f)$ for crack radii between 2mm and 2.5mm. Next the differences between $\sigma_S(f)$ and $\sigma_K(a, f)$ summed over the frequency range is calculated as the crack radius, a is varied, and is denoted by

$$D(a) = ||\sigma_S(f) - \sigma_K(a, f)||_2. \tag{69}$$

Figure 11 plots $D(a)$ as the crack radius, a, is varied within the model and shows a clear minimum for $a = 2.2$mm (again the frequency range used was 0.75-2.25 MHz). The actual crack radius in the simulation is 2.5mm and so the percentage error in the value recovered using the maximum eigenvalue method is 12%, which is a reasonable error considering the assumptions within the model and the effects within the simulation which are not included within the model.

7   Conclusions

In this paper a formula which relates the maximum eigenvalue from a scattering matrix to the length of a crack within an elastic solid was presented. This formula shows that there is a one to one relationship between the two and that this can be used to tackle the inverse problem of objectively sizing a crack in an elastic solid given the ultrasonic array output data. The
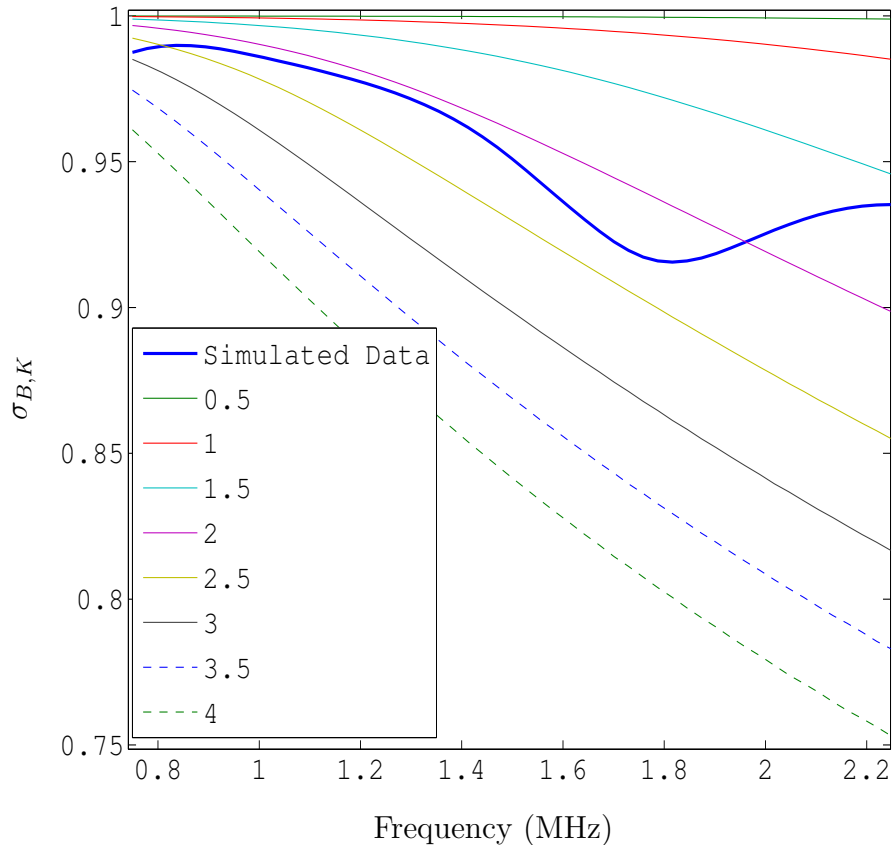
31

Figure 10: This plot shows the maximum eigenvalue, $\sigma_S(f)$, from the scattering matrices extracted from the simulated data (thick blue line) as a function of frequency and compares this with the maximum eigenvalue, $\sigma_K(a, f)$ from the scattering matrices determined using the Kirchhoff model as a function of frequency for different crack radii.

Kirchhoff model was used to approximate the scattering matrices which arise when a linear elastic wave encounters a crack within a homogeneous medium. The scattering matrix from the model was approximated by a Toeplitz matrix and an upper bound to the maximum eigenvalue from this Toeplitz matrix was used to derive an explicit relationship between the maximum eigenvalue and the crack radius over the wavelength $\hat{a} = a/\lambda$. The sensitivity of the maximum eigenvalue approximation, σ_B, to changes in the system parameters was also examined. From this analysis it was concluded
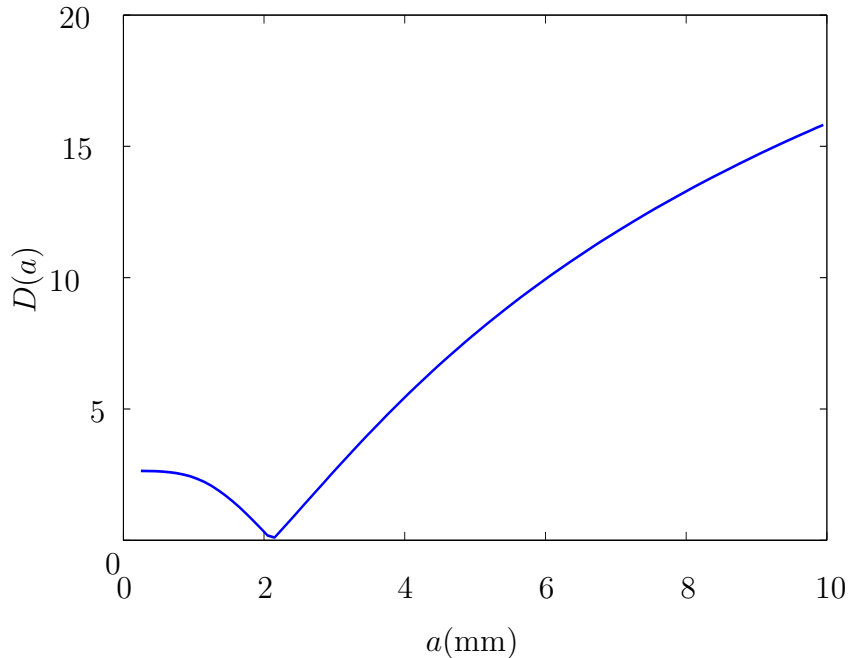
Figure 11: This plot shows the sum of the absolute differences, $D(a)$ (equation (69)), over a range of frequencies (0.75 -2.25 MHz) between the maximum eigenvalue from the scattering matrices from the simulated data, $\sigma_S(f)$, and the Kirchhoff model, $\sigma_K(a, f)$, as the crack radius, a, is varied within the model.

that σ_B is most sensitive to changes in $\hat{a}$ when $\hat{a} < 0.8$ and there is little change in σ_B for $\hat{a} > 0.8$. This implies that the method of using the maximum eigenvalue to determine the size of a crack in a homogeneous material (the inverse problem) is most effective when the crack is of similar length to the wavelength (that is, when $\hat{a} \approx 0.5$). For much larger cracks another method should be adopted such as an image-based method (for example the TFM). In addition, it was observed that errors in the measured length of the array, depth of the flaw, and number of elements has little effect on the inverse problem. Finally the method was applied to time domain FMC data from a finite element simulation and the crack size was objectively recovered exhibiting an error of 12%.

Appendices

A   Toeplitz Matrix Approximation

The aim here is to show that each row of $N/2$ elements starting at the specular reflection diagonal is approximately equal to the row of $N/2$ elements where the maximum occurs, $A(y_{N/2+1}, y_n)$, and so justify the Toeplitz approximation. From equation (10)

$$y_{n-m+N/2+1} + y_m = \frac{\triangle y}{2}(N - 2n) \tag{70}$$

and also

$$y_{N/2+1} + y_n = y_n - \frac{\triangle y}{2} = \frac{\triangle y}{2}(N - 2n). \tag{71}$$

Hence, from equation (15)

$$A_{N/2+1,n} = \frac{2\sqrt{1 - \triangle y^2/4}}{\rho c^2 \triangle y(2n - N)}\left(L + 2\mu\left(1 - \frac{\triangle y^2}{4}(N - 2n + 1)^2\right)\right)J_1(\pi \hat{a}\triangle y(2n-N)), \tag{72}$$

and

$$A_{m,n-m+N/2+1} = \frac{2\sqrt{1 - \triangle y^2/4(N - 2m + 1)^2}}{\rho c^2 \triangle y(2n - N)}\left(L + 2\mu\left(1 - \frac{\triangle y^2}{4}\left(\frac{N}{2} - 2n + 2m - 1\right)^2\right)\right)$$

$$\times J_1(\pi \hat{a}\triangle y(2n - N)) \tag{73}$$

which gives

$$A_{N/2+1,n} - A_{m,n-m+N/2+1} = \frac{J_1\left(\pi\hat{a}\triangle y(2n-N)\right)}{\rho c^2 \triangle y(2n-N)} \left(2\sqrt{1-\frac{\triangle y^2}{4}}\right.$$

$$\times \left(L + 2\mu\left(1 - \frac{\triangle y^2}{4}(N-2n+1)^2\right)\right)$$

$$- 2\sqrt{1 - \frac{\triangle y^2}{4}(N-2m+1)^2}$$

$$\left.\left(L + 2\mu\left(1 - \frac{\triangle y^2}{4}\left(\frac{N}{2} - 2n + 2m - 1\right)^2\right)\right)\right).$$

(74)

If we let

$$\chi = L + 2\mu\left(1 - \frac{\triangle y^2}{4}(N - 2n + 1)^2\right)$$

(75)

then equation (74) becomes

$$A_{N/2+1,n} - A_{m,n-m+N/2+1} = \frac{J_1(\pi\hat{a}\triangle y(2n-N))}{\rho c^2 \triangle y(2n-N)} \left(2\sqrt{1-\frac{\triangle y^2}{4}}\chi\right.$$

$$- 2\sqrt{1 - \frac{\triangle y^2}{4}(N-2m+1)^2}\left(\chi - \frac{\mu\triangle y^2}{2}\left(\left(\frac{N}{2} - 2m + 2\right)^2\right.\right.$$

$$\left.\left.\left.- 2\left(\frac{N}{2} - 2m + 2\right)(N - 2n + 1)\right)\right)\right).$$

(76)

Now since $m \in [N/2 + 1, N]$ then the maximum that $|\triangle y/2(N - 2m + 1)|$ can achieve is when $m = N$ and so this is bounded by

$$\left(-\frac{\triangle y(N-1)}{2}\right)^2 = \frac{l^2}{4(4d^2 + l^2)} = \epsilon$$

(77)

where $0 < \epsilon \ll 1$ for small apertures. This then allows the Taylor series expansion

$$\sqrt{1 - \left(\frac{\triangle y}{2}(N - 2m + 1)\right)^2} = 1 - \frac{\epsilon}{2} + \mathcal{O}(\epsilon^2).$$

(78)

In addition, for $m = N$ and $n = N/2 + 1$ the following approximation is

made within equation (76) to give

$$
\frac{\triangle y^2}{2} \left(\left(\frac{N}{2} - 2m + 1 \right)^2 + 2 \left(\frac{N}{2} - 2m + 2 \right) (N - 2n + 1) \right)
$$

$$
= \frac{\triangle y^2}{2} \left(\left(\frac{3N}{2} - 1 \right)^2 - 2 \left(\frac{3}{N} - 2 \right) \right)
$$

$$
= \frac{9}{2} \frac{\triangle y^2}{4} \left(N^2 - \frac{8}{3} N + \frac{20}{9} \right)
$$

$$
\approx \frac{9}{2} \mathcal{O}(\epsilon). \tag{79}
$$

for large N (as the N^2 term dominates) and from equation (77)

$$
\frac{\triangle y^2}{4} N^2 = \mathcal{O}(\epsilon). \tag{80}
$$

Substituting the approximations given by equations (78) and (79) into equation (76) gives

$$
A_{N/2+1,n} - A_{m,n-m+N/2+1} = \frac{J_1(\pi \hat{a} \triangle y(2n - N))}{\rho c^2 \triangle y(2n - N)} \left(2\chi - 2 \left(1 - \frac{\epsilon}{2} \right) (\chi + \mu\epsilon) \right)
$$

$$
= \frac{2 J_1(2\pi \hat{a} \triangle y(N/2 + 1 - n))}{\rho c^2 \triangle y(2n - N - 2)} (\epsilon(\chi + \mu\epsilon - 2\mu)) \tag{81}
$$

where $\sqrt{1 - (\triangle y)^2/4} \approx 1$ since $0 < \triangle y \ll \epsilon$. In order to obtain the relative error, equation (81) is divided by

$$
A_{N/2+1,n} = \frac{2 J_1(\pi \hat{a} \triangle y(2n - N))}{\rho c^2 \triangle y(2n - N)} \chi \tag{82}
$$

to give

$$
\left| \frac{A_{N/2+1,n} - A_{m,n+m-N/2+1}}{A_{N/2+1,n}} \right| = \epsilon - \frac{2\mu}{\chi} \epsilon + \frac{\mu}{\chi} \epsilon^2
$$

$$
= \mathcal{O}(\epsilon) \tag{83}
$$

since $\chi = \mathcal{O}(\mu)$ from equation (75) and therefore $\mu/\chi \approx 1$. Hence the approximation of the limited aperture scattering matrix by a Toeplitz matrix is justified here.

B   Determining the transition parameter t^*

In section 4.1 the Bessel function in equation (23) is approximated by two expansions, one for small arguments and one for large arguments, as given by equations (26) and (27). The parameter t^* is the index which determines when the argument transitions from small to large. If we denote the argument in the Bessel function by T then at $t = t^*$

$$T = 2\pi\hat{a} \left(\frac{\triangle y}{2} \left(N - 2t^* \right) \right) \tag{84}$$

from equation (10). Rearranging gives

$$t^*(\hat{a}) = \frac{N}{2} - \frac{T}{2\pi\hat{a}\triangle y}. \tag{85}$$

The higher order terms from the approximations in equations (26) and (27) are used to find a suitable numerical value for T. These are given by

$$E_1(t,\hat{a}) = \left| \frac{1}{384} \left(\pi\hat{a} \left(y_t - \frac{\triangle y}{2} \right) \right)^4 \right| \tag{86}$$

and

$$E_2(t,\hat{a}) = \left| \frac{3}{24\pi^2} \sin\left(2\pi\hat{a} \left(y_t - \frac{\triangle y}{2} \right) - \frac{3\pi}{4} \right) \left(2\pi\hat{a} \left(y_t - \frac{\triangle y}{2} \right) \right)^{-\frac{5}{2}} \right|. \tag{87}$$

A function $\hat{t}^*(\hat{a})$ is introduced and is taken to be the array element index, n, closest to the point of intersection of the functions $E_1(t, \hat{a})$ and $E_2(t, \hat{a})$, that is

$$\hat{t}^*(\hat{a}) = \max_{E_1(t,\hat{a})>E_2(t,\hat{a})} t \qquad \text{if } t \in [N/2+2, N]. \tag{88}$$

As the error functions given by (30) and (90) are monotonically increasing in t then, by taking $t = t^*$ for all t, the following upper bounds can be derived.

$$e_1 = \frac{\hat{a}^4}{384}\left(y_{t^*} - \frac{\triangle y}{2}\right)^4 w_{t^*}(N)F_{t^*}(\hat{a})(t^* - N/2) \tag{89}$$

and similarly setting $t = N$ for all t gives the upper bound

$$e_2 = \frac{3}{24\pi^3}\left(\hat{a}\left(y_N - \frac{\triangle y}{2}\right)\right)^{-\frac{5}{2}}\sin\left(2\pi\hat{a}\left(y_N - \frac{\triangle y}{2}\right) - \frac{3\pi}{4}\right)F_N(\hat{a})w_N(N)(N-t^*). \tag{90}$$

C   Approximating the Upper Bound on the Maximum Eigenvalue

To justify the removal of the floor function it necessary to show that

$$\cos\left(\alpha_1\right) - \cos\left(\alpha_2\right) = \epsilon, \tag{91}$$

for $0 < \epsilon \ll 1$, where

$$\alpha_1 = \frac{\pi}{2(N-1)/(2t-2-N)+2} \qquad \text{and} \qquad \alpha_2 = \frac{\pi}{2(N-1)/(2t-2-N)+3}, \tag{92}$$

since the maximum error that occurs with the floor function is 1. The range of t is $t = N/2 + 2, ..., N$ which gives

$$\frac{2(N-1)}{2t-2-N} = N-1, \frac{N-1}{2}, ..., \frac{2(N-1)}{N-2}$$
$$\approx N-1, \frac{N-1}{2}, ..., 2 \tag{93}$$

for large N and so the ranges of α_1 and α_2 are

$$\alpha_1 = \frac{\pi}{N+1}, ..., \frac{\pi}{4} \tag{94}$$

and

$$\alpha_2 = \frac{\pi}{N+2}, ..., \frac{\pi}{5}, \tag{95}$$

and therefore $0 < \alpha_1, \alpha_2 < \pi/2$. The derivative of $\cos(\alpha_i)$ is maximised at $\pi/2$ and minimised at 0 and therefore the maximum difference between $\cos(\alpha_1)$ and $\cos(\alpha_2)$ occurs when $t = N$ and is such that

$$\epsilon = \cos\left(\frac{\pi}{4}\right) - \cos\left(\frac{\pi}{5}\right)$$
$$= \mathcal{O}(10^{-1}). \tag{96}$$

D   Sensitivity of the maximum eigenvalue to the system parameters

In order to analytically assess the sensitivity of the maximum eigenvalue to changes in the system parameters, such as the number of elements in the array N, the length of the array l, the depth of the flaw d and $\hat{a}$, it is necessary to determine the derivatives in the following expression for the

relative change in σ_B,

$$\frac{\triangle\sigma_B}{\sigma_B} = \frac{\partial\sigma_B}{\partial\hat{a}}\frac{\hat{a}}{\sigma_B}\frac{\triangle\hat{a}}{\hat{a}} + \frac{\partial\sigma_B}{\partial N}\frac{N}{\sigma_B}\frac{\triangle N}{N} + \frac{\partial\sigma_B}{\partial l}\frac{l}{\sigma_B}\frac{\triangle l}{l} + \frac{\partial\sigma_B}{\partial d}\frac{d}{\sigma_B}\frac{\triangle d}{d}. \quad (97)$$

The expression given by

$$\frac{\partial\sigma_B}{\partial\hat{a}}\frac{\hat{a}}{\sigma_B} \quad (98)$$

in equation (97) provides a relative measure of how sensitive σ_B is to changes in the crack size. This provides a guide as to how useful this method will be in practice in recovering the crack size from a given maximum eigenvalue (the so called inverse problem). This sensitivity is dependent on the other system parameters and the effects of these will be examined in this section. The other three components in equation (97)

$$\frac{\partial\sigma_B}{\partial N}\frac{N}{\sigma_B}, \qquad \frac{\partial\sigma_B}{\partial l}\frac{l}{\sigma_B} \qquad \text{and} \qquad \frac{\partial\sigma_B}{\partial d}\frac{d}{\sigma_B} \quad (99)$$

determine the errors that occur in σ_B as a result of errors in the system parameters; N, l and d. In this section the derivatives contained in each of these components will be calculated and numerically interpreted to analyse the sensitivity of the method.

From equation (64) the derivative of σ_B with respect to $\hat{a}$ is given by

$$\frac{\partial\sigma_B}{\partial\hat{a}} = (\hat{A} + \hat{S}_1(\hat{a})) + \frac{\partial\hat{S}_1}{\partial\hat{a}}\hat{a} + 3\hat{S}_2(\hat{a})\hat{a}^2 + \frac{\partial\hat{S}_2}{\partial\hat{a}}\hat{a}^3 + \frac{\partial Q(\hat{a})}{\partial\hat{a}}\cos(p(\hat{a}) - \phi(\hat{a}))$$
$$- Q(\hat{a})\sin(\hat{p}(\hat{a}) - \phi(\hat{a}))\left(\frac{\partial p}{\partial\hat{a}} - \frac{\partial\phi}{\partial\hat{a}}\right). \quad (100)$$

The expression given by equation (98) gives the relative error in the maximum eigenvalue σ_B for a relative change in the crack radius over the wavelength, $\hat{a}$. Figure 12 shows this relative error as each of the parameters is varied. Figure 12 (a) shows that for $\hat{a} < 0.8$ the relative derivative is close
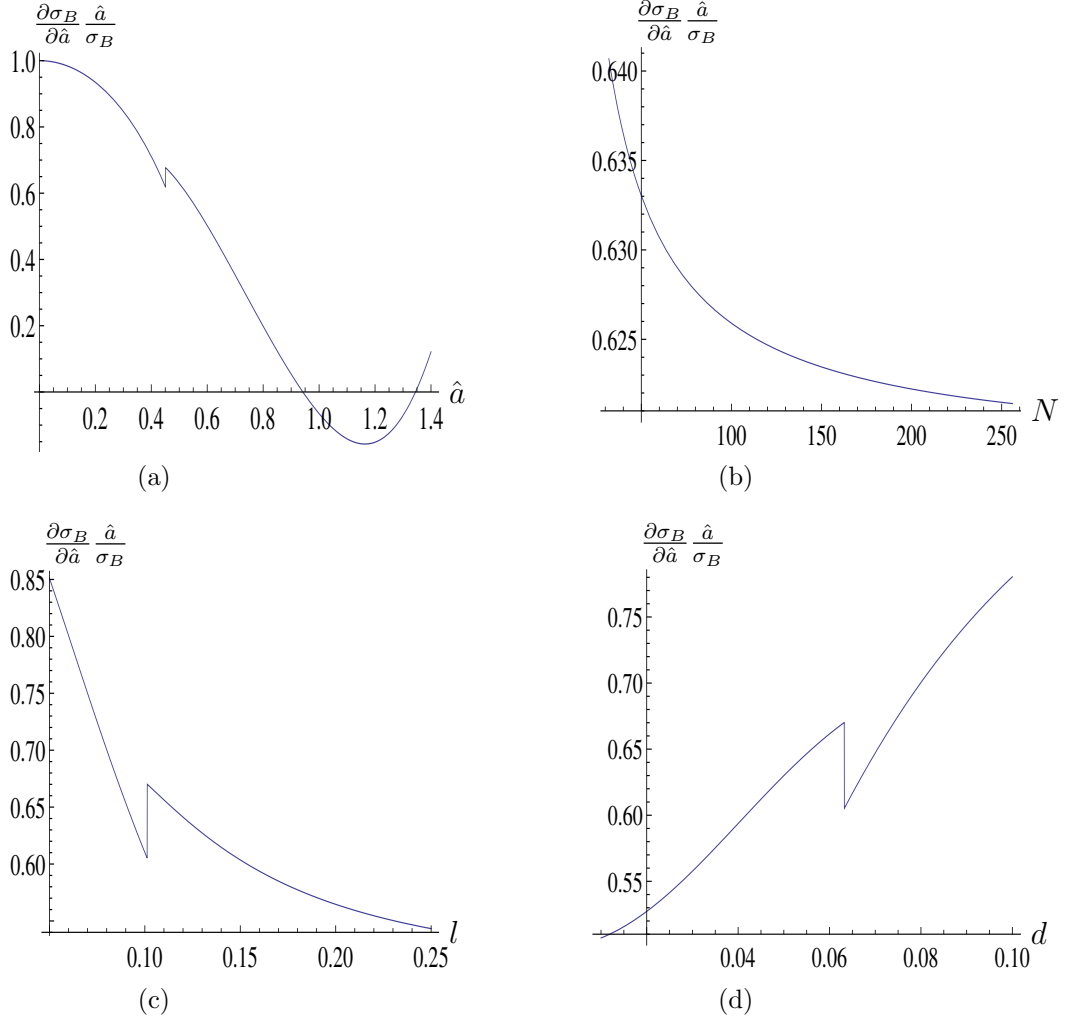
Figure 12: The relative derivative of the maximum eigenvalue, σ_B, with respect to $\hat{a}$, equation (98), as a function of (a) $\hat{a}$, (b) N, (c) l and (d) d, where all other parameters fixed at $\hat{a} = 0.5$, $N=64$, $l=128$mm and $d=50$mm in each respective case.

to one which illustrates that changes in σ_B are sensitive to changes in $\hat{a}$. This is encouraging as it indicates that this crack sizing method is sensitive to changes in σ_B for cracks that are close to or below the wavelength. For $\hat{a} > 0.8$ the relative derivative is small and so the method is not very sensitive for larger values of $\hat{a}$. This result implies that this method should be used for sizing cracks commensurate with the wavelength (that is when $\hat{a} \approx 0.5$, recall $\hat{a}$ is the crack radius over wavelength) and when $\hat{a} > 0.8$ another

method should be adopted; perhaps an image-based method. Figures 12 (b), (c) and (d) show that $(\partial \sigma_B / \partial \hat{a}) \cdot (\hat{a}/\sigma_B)$ is reasonably constant as the number of elements N (Figure 12 (b)), the length of the array l (Figure 12 (c)) and the depth of the flaw d (Figure 12 (d)) are varied. This implies that the crack sizing capability of the maximum eigenvalue method is relatively insensitive to changes in these parameters. Examining now the second of the terms in equation (97) the derivative of σ_B with respect to the number of elements N is given by

$$\frac{\partial \sigma_B}{\partial N} = (\frac{\partial \hat{S}_1}{\partial \hat{A}} + \frac{\partial \hat{S}_1}{\partial N})\hat{a} + \frac{\partial \hat{S}_2}{\partial N}\hat{a}^3 + \frac{\partial Q}{\partial N}\cos(p(\hat{a}) - \phi(\hat{a})) - Q(\hat{a})\left(\frac{\partial p}{\partial N} - \frac{\partial \phi}{\partial N}\right)\sin(p(\hat{a}) - \phi(\hat{a})).$$
(101)

Figure 13 plots the relative derivative

$$\frac{\partial \sigma_B}{\partial N}\frac{N}{\sigma_B}$$
(102)

as (a) $\hat{a}$, (b) N, (c) l and (d) d are varied. These plots show that for each of the parameters ($\hat{a}, N, l$ and d) the value of the expression given in equation (102) is pretty much constant and roughly equally to 1. In reality the error in the number of elements in the array will be zero as this should be known with certainty within an experiment.

Turning now to the third term in equation (97), the derivative of σ_B with respect to the length of the array, l, is given by

$$\frac{\partial \sigma_B}{\partial l} = (\frac{\partial \hat{A}}{\partial l} + \frac{\partial \hat{S}_1}{\partial l})\hat{a} + \frac{\partial \hat{S}_2}{\partial l}\hat{a}^3 + \frac{\partial Q}{\partial l}\cos(p(\hat{a}) - \phi(\hat{a})) - Q(\hat{a})\left(\frac{\partial p}{\partial l} - \frac{\partial \phi}{\partial l}\right)\sin(p(\hat{a}) - \phi(\hat{a})).$$
(103)

Figure 14 shows the relative derivative,

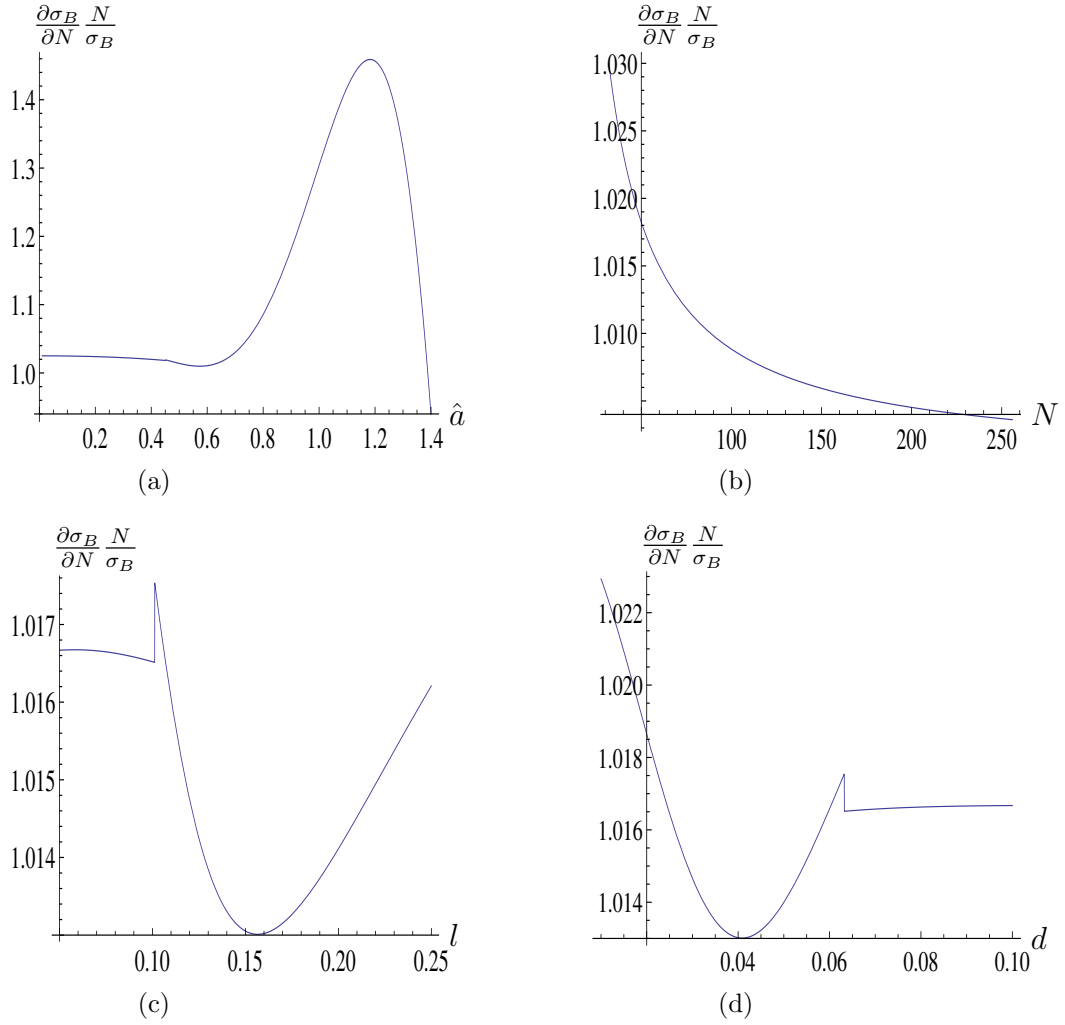$$\frac{\partial \sigma_B}{\partial l}\frac{l}{\sigma_B}$$
(104)

42

Figure 13: The relative derivative of the maximum eigenvalue, σ_B, with respect to N, equation (102)is plotted as (a) $\hat{a}$, (b) N, (c) l and (d) d are varied, with all other parameters fixed at $\hat{a} = 0.5$, N=64, l=128mm and d=50mm in each case.

which gives the relative change, σ_B, caused by a relative error in the length of the array, l, as (a) $\hat{a}$, (b) N, (c) l and (d) d are varied. These plots show that the change in σ_B, due to an error in the measured length of the array l, is negligible; plots (a)-(d) show that the expression in equation (104) is of the order 10^{-1} as each of the parameters ($\hat{a}$, N, l and d) are varied. This is encouraging as it means that the inverse problem of recovering the size of the crack using this method is not sensitive to errors in the length of the
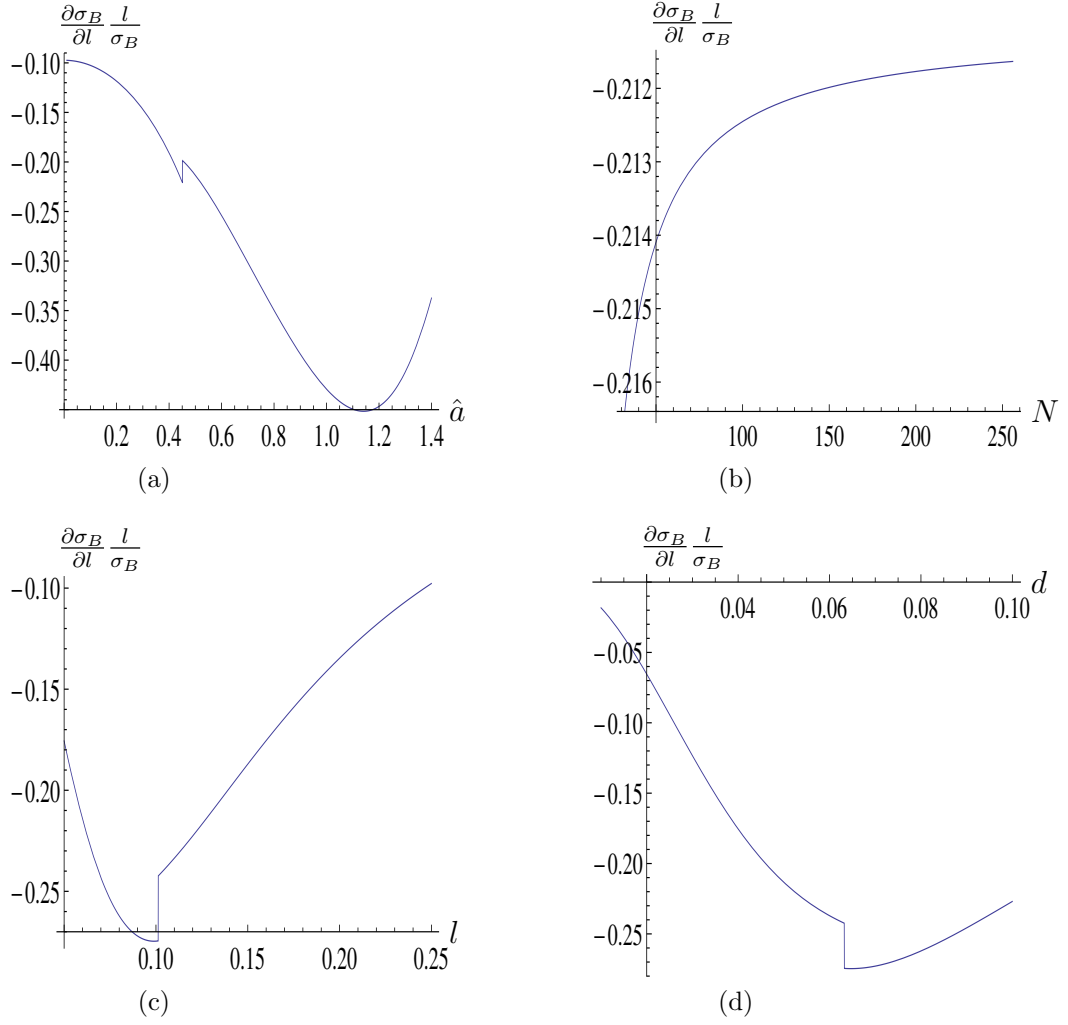
Figure 14: The relative derivative of the maximum eigenvalue, σ_B, with respect to l, equation (104), is plotted as (a) $\hat{a}$, (b) N, (c) l and (d) d are varied, with all other parameters fixed at $\hat{a} = 0.5$, $N=64$, $l=128$mm and $d=50$mm in each case.

array.

Finally, σ_B is differentiated with respect to the depth of the crack, d, and is given by

$$\frac{\partial \sigma_B}{\partial d} = \left(\frac{\partial \hat{A}}{\partial d} + \frac{\partial \hat{S}_1}{\partial d} \right) \hat{a} + \frac{\partial \hat{S}_2}{\partial d} \hat{a}^3 + \frac{\partial Q}{\partial d} \cos(p(\hat{a}) - \phi(\hat{a})) - Q(\hat{a}) \left(\frac{\partial p}{\partial d} - \frac{\partial \phi}{\partial d} \right) \sin(p(\hat{a}) - \phi(\hat{a})).$$
$$(105)$$

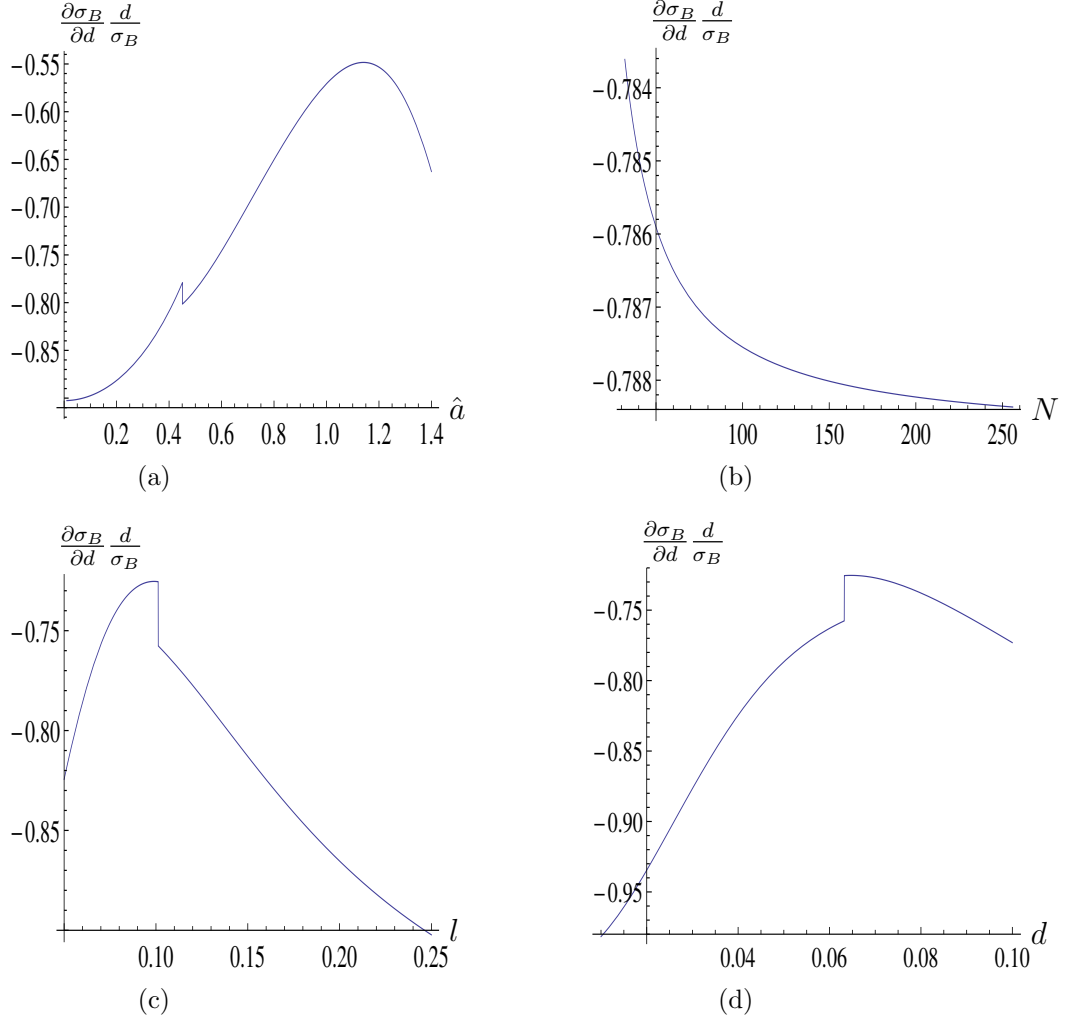The relative error in σ_B caused by a relative error in the depth of the

44

Figure 15: The relative derivative of the maximum eigenvalue, σ_B, with respect to d, equation (106) is plotted as a function of (a) $\hat{a}$, (b) N, (c) l and (d) d, with all other parameters fixed at $\hat{a} = 0.5$, $N=64$, $l=128$mm and $d=50$mm in each case.

flaw, d, is shown in Figure 15 where

$$\frac{\partial \sigma_B}{\partial d} \frac{\triangle d}{\sigma_B} \tag{106}$$

is plotted as a function of (a) $\hat{a}$, (b) N, (c) l and (d) d. Again, it is clear from these figures that there will be little error in σ_B resulting from an error in d as the expression in equation (106) is approximately constant and of

45

the order 10^{-1} for each of the parameters varied in Figure 15 (a)-(d).

References

[1] C. Hellier. *Handbook of Nondestructive Evaluation*. McGraw Hill Professional, New York, USA, 2012.

[2] R.D. Adams and P. Cawley. A review of defect types and non destructive testing techniques for composites and bonded joints. *NDT &E Int.*, 21(4):208–222, 1988.

[3] L. Cheng and G.Y. Tian. Pulsed electromagnetic *NDE* for defect detection and characterisation in composites. *IEEE Int. Instrumentation and Measurement Technology Conference*, pages 1902–1907, 2012.

[4] A. Ettemeyer. Laser shearography for inspection of pipelines. *Nuclear Engineering and Design*, 160:237–240, 1996.

[5] J.L. Rose. *Ultrasonic Waves in Solid Media*. Cambridge University Press, Cambridge, UK, 1999.

[6] L. Schmerr and S. Song. *Ultrasonic Nondestructive Evaluation Systems*. Springer, NY, USA, 2010.

[7] A. Safari and E.K. Akdo gan. *Piezoelectric and Acoustic Materials for Transducer Applications*. Springer, NY, USA, 2008.

[8] B.W. Drinkwater and P.D. Wilcox. Ultrasonic arrays for nondestructive evaluation: A review. *NDT & E Int*, 39(7):525–541, 2006.

[9] G.D. Connolly, M.J.S. Lowe, S.I. Rokhlin, and J.A.G. Temple. Imaging of defects within austenitic steel welds using an ultrasonic array. *AIP Conference Proceedings, Illinois, Chicago*, 1096, 22-25 July 2009.

[10] P.D. Wilcox, C. Holmes, and B.W. Drinkwater. Advanced reflector characterization with ultrasonic phased arrays in *NDE* applications. *IEEE TUFFC*, 38(8):701–711, 2005.

[11] J. Zhang, B.W. Drinkwater, P.D. Wilcox, and A.J. Hunter. Defect detection using ultrasonic arrays: The multi-mode total focusing method. *NDT & E Int*, 43(2):123–133, 2010.

[12] C. Holmes, B.W. Drinkwater, and P.D. Wilcox. Post processing of the full matrix of ultrasonic transmit receive array data for non destructive evaluation. *NDT & E Int*, 38(8):701–711, 2005.

[13] A. Velichko and P.D. Wilcox. An analytical comparison of ultrasonic array imaging algorithms. *JASA*, 127(4):2378–2384, 2010.

[14] C. Fan, M. Caleap, M. Pan, and B.W. Drinkwater. A comparison between ultrasonic array beamforming and super resolution imaging algorithms for non-destructive evaluation. *Ultrasonics*, 54:1842–1850, 2014.

[15] J. Zhang, B.W. Drinkwater, and P.D. Wilcox. Effects of array transducer inconsistencies on total focusing method imaging performance. *NDT & E Int.*, 44:361–368, 2011.

[16] J. Zhang, B.W. Drinkwater, and P.D. Wilcox. Comparison of ultrasonic array imaging algorithms for nondestructive evaluation. *IEEE TUFFC*, 60(8):1732–1745, 2013.

[17] A. Velichko and P. Wilcox. Reversible back-propagation imaging algorithm for postprocessing of ultrasonic array data. *IEEE TUFFC*, 56(11):2492–2264, 2009.

[18] J. Zhang, B.W. Drinkwater, and P.D. Wilcox. Defect characterization using an ultrasonic array to measure the scattering coefficient matrix. *IEEE TUFFC*, 55(10):2254–2264, 2008.

[19] C. Li, D. Pain, P.D. Wilcox, and B.W. Drinkwater. Imaging composite material using ultrasonic arrays. *NDT & E Int.*, 53:8–17, 2013.

[20] J. Zhang, B.W. Drinkwater, and P.D. Wilcox. Effect of roughness on imaging and sizing rough crack-like defects using ultrasonic arrays. *IEEE TUFFC*, 59(5):939–948, 2012.

[21] J. Zhang, B.W. Drinkwater, and P.D. Wilcox. Longitudinal wave scattering from rough crack-like defects. *IEEE TUFFC*, 58(10):2171–2179, 2011.

[22] A.J. Hunter, B.W. Drinkwater, and P.D. Wilcox. Least-squares estimation of imaging parameters for an ultrasonic array using known geometric image features. *IEEE TUFFC*, 58(2):414–426, 2011.

[23] A.J. Hunter, B.W. Drinkwater, and P.D. Wilcox. The wavenumber algorithm for full matrix imaging using an ultrasonic array. *IEEE Trans. Ultrason. Ferroelectr. Freq. Control*, 55(11):2450–2462, 2008.

[24] K. M. M. Tant, A. J. Mulholland, and A. Gachagan. Ultrasonic characterization of crack-like defects using scattering matrix similarity metrics. *Ultrasonics, Ferroelectrics, and Frequency Control, IEEE Transactions on*, 62(5):915–926, 2015.

[25] J. Zhang, B.W. Drinkwater, and P.D. Wilcox. The use of ultrasonic arrays to characterize crack-like defects. *J Nondestructive Eval*, 29(4):222–232, 2010.

[26] L. Bai, A. Velichko, and B. Drinkwater. Ultrasonic characterization of crack-like defects using scattering matrix similarity metrics. *Ultrasonics, Ferroelectrics, and Frequency Control, IEEE Transactions on*, 62(3):545–559, 2015.

[27] L. W.Schmerr. *Fundamentals of Ultrasonic Nondestructive Evaluation: A Modelling Approach.* Plenum Press, New York, 1998.

[28] D. Hertz. Simple bounds on the extreme eigenvalues of toeplitz matrices. *IEEE Trans. Inform. Theory.*, 38(1):175–176, 1992.

[29] M. Abramowitz and I.A. Stegun. *Handbook of Mathematical Functions with Formulas, Graphs and Mathematical Tables.* Dover Publications, New York, USA, 1972.

[30] T. Arakawa, T. Ibukiyama, M. Kaneko, and D. Zagier. *Bernoulli numbers and zeta functions.* Springer, 2014.

[31] PZFlex Weidlinger Associates Inc. 399 West El Camino Real Mountain View CA 94040-2607.